



OPEN

## Origin of mysterious geothermal gas emissions in the middle of the Western Desert, stable shelf area, Dakhla Oasis, Egypt

Mohamed Abdel Zaher<sup>1✉</sup>, Mahmoud El-Hadidy<sup>1</sup>, Gad El-Qady<sup>1</sup>, Taha Rabeh<sup>1</sup>, Magdy Atya<sup>1</sup>, Sherif El-hady<sup>1</sup>, Abdel Aziz Tantawy<sup>2</sup>, Ibrahim El-Hemaly<sup>1</sup>, Mohamed Al Deep<sup>1</sup>, Ahmed Awad<sup>1</sup>, Hamada Salama<sup>1</sup>, Mohamed Mostafa Khalifa<sup>1</sup> & Mahmoud Leila<sup>3</sup>

This work responds to what was reported in various audio-visual media channels and to queries and explanations from individuals and local residents on the causes of gaseous and thermal emissions from the Earth near the vicinity of the village of Al-Hindaw in Dakhla city, New Valley Governorate, Egypt. At the location of the fume exit area, magnetic, seismic, and electromagnetic geophysical investigations were carried out to identify the factor(s) responsible for the event in question. Rock samples were collected and studied geochemically and radiographically to assess their chemical compositions, as well as the quantity of organic chemicals that may have contributed to the burning and temperature increase. In light of the results of the geochemical and geophysical research, it is believed that the self-ignitions are the result of near-surface reactions and oxidation instead of volcanic activity, such as the presence of magma or other comparable phenomena.

The village of Al-Hindaw in Dakhla city (Fig. 1), New Valley Governorate, Egypt, has witnessed a strange phenomenon: the emergence of warm gas emissions ( $> 100\text{ }^{\circ}\text{C}$ ) accompanied by the precipitation of sulfur. It occurs in the area of Al-Hindaw-Mutt Road, approximately 1.5 km from the city of Mut and 2.5 km from the village of Al-Hindaw (Fig. 1). This phenomenon has drawn the attention of various media outlets, which has led to widespread panic among local people. The phenomenon was not confined to this particular locale alone; it was witnessed at more than one location in the general vicinity of the Al-Hindaw region. It commonly arises after excavation work has been done, whether by people or by governments, for the purpose of constructing houses and other infrastructure. Similar hot geothermal emissions have been reported from different places around the world (e.g., Italy, Iceland, Ethiopia, Japan and Mexico). Most of these emissions are associated with hot fluids commonly enriched in  $\text{CH}_4$ ,  $\text{CO}_2$ ,  $\text{N}_2$  and  $\text{H}_2$  gases<sup>1–7</sup>. Gas-rich geothermal emissions are often associated with unique geological processes, such as volcanism, fluid–rock interactions and organic matter maturation<sup>6,8–10</sup>.

The phosphate mines in Quseir and Safaga experienced self-ignition fires due to their high concentrations of hydrocarbons and pyrite<sup>12</sup>. A significant temperature gradient was observed in the Abu Tarture area ( $74\text{ m km}^{-1}$ ), which they attributed to the 80–150 m-deep oxidative heating of pyrite in the phosphate deposit<sup>13</sup>.

Therefore, it was essential to study the phenomenon of self-ignition in the Al-Hindaw area and discover its causes using geochemical and geophysical investigations. A preliminary expedition was conducted as a part of the present research prior to commencing any field surveys. The primary objective of this journey was to acquire comprehensive knowledge about the attributes of the phenomenon being examined, as well as to determine the geophysical methodologies that are the most suitable for the specific region of interest. Consequently, the research methodology was developed based on the geographical situation of the area and the character of the phenomenon being studied. Several geophysical methods were used to conduct field measurements in the study region, including terrestrial magnetic, seismic refraction, multichannel analysis of surface waves (MSW), time-domain electromagnetic (TEM), and very low frequency (VLF) methods. The purpose of these approaches is to establish the kind of rock succession in the area of study, the influence of spontaneous combustion, and the degree to which it extends under the strata, as well as whether there is evidence of subsurface faults, fractures or any seismic activity. Additionally, geochemical studies, organic petrography, and organic geochemical analyses

<sup>1</sup>National Research Institute of Astronomy and Geophysics (NRIAG), Helwan, Cairo 11421, Egypt. <sup>2</sup>New Valley Vertebrate Palaeontology Centre, New Valley University, New Valley, Egypt. <sup>3</sup>Geology Department, Faculty of Science, Mansoura University, Mansoura 35516, Egypt. ✉email: moh\_zaher@nriag.sci.eg

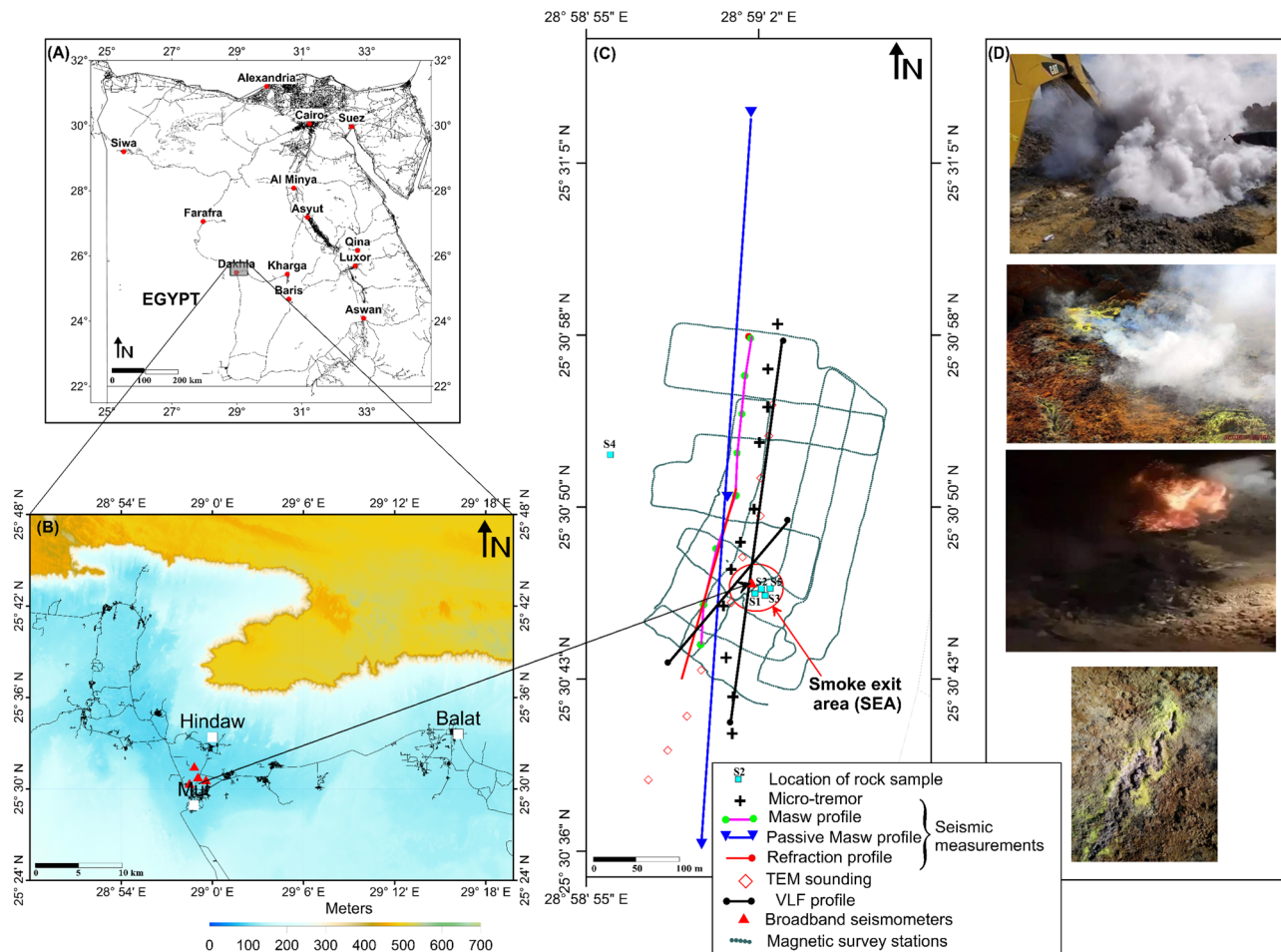


**Figure 1.** (A) A map of Egypt illustrating the position of the Dakhla Oasis in the middle of the Western Desert. (B) Topographic map of the Dakhla Oasis relying on a digital surface model (DSM) with an approximate 30-m spatial resolution<sup>11</sup>. (C) The location of geophysical surveys as well as rock samples for geochemical study in/ around the smoke exit area (SEA). (D) Photographs captured from the locations where smoke and flames are emanating.

were performed, as well as gas collection and analysis. The results of the geochemical analysis will provide us with information on the chemical and mineral compositions of the rocks, including the percentage of organic compounds present, whether or not radioactive elements are present, and the source of the gases that are being released. The relevance of this study is in understanding the characteristics of the phenomena of natural combustion in order to provide reassurance to the people and facilitate its optimum use. Additionally, it aims to assess the potential risks posed to the local population via an analysis of the released gases.

### Geological and structural settings and seismicity

The Dakhla Basin, which includes the Dakhla Oasis, is a large sedimentary basin in the middle of the Western Desert. It consists of a very thick and well-exposed Upper Cretaceous–lower Palaeogene succession<sup>14</sup>. The Dakhla Oasis stretches 70 km from west to east and up to 20 km from north to south. Its margins are visible only in the north, where the limestone plateau's massive steep escarpment forms a prominent ridge, while the south is fully open. East of the Dakhla Oasis is a dune-covered plain that extends along the Kharga–Dakhla road<sup>15</sup>. To the north of the Dakhla depression, a high-level limestone plateau reaches a significant distance beyond the oasis<sup>16</sup>. The regional dip of the layers that comprise the Dakhla Oasis is to the north, resulting in the formation of quistas along the boundary between the southern Nubian sandstone and the northern Cretaceous shales and Palaeocene chalk (Fig. 2).

As stated by Said<sup>16</sup>, the area under investigation is a portion of the stable shelf, which mainly consists of the horizontal strata that comprise the Western Desert terrain. Thus, elements of the Dakhla Basin's structure are characteristic of those formed by stable shelf tectonics, which are characterized by gentle tectonic deformations, and the majority of its sedimentary cover is made up of continental as well as epicontinental deposits. Said ruled out tectonic origins for the Western Desert depressions and thought that the Dakhla depression was located in plateaus that did not experience considerable tensional strains during ascent<sup>18</sup>. According to Klitzsch et al.<sup>19</sup>, the average thickness of the Nubian Group on the southern edge of the Dakhla Basin lies between 1000 and 2000 m,

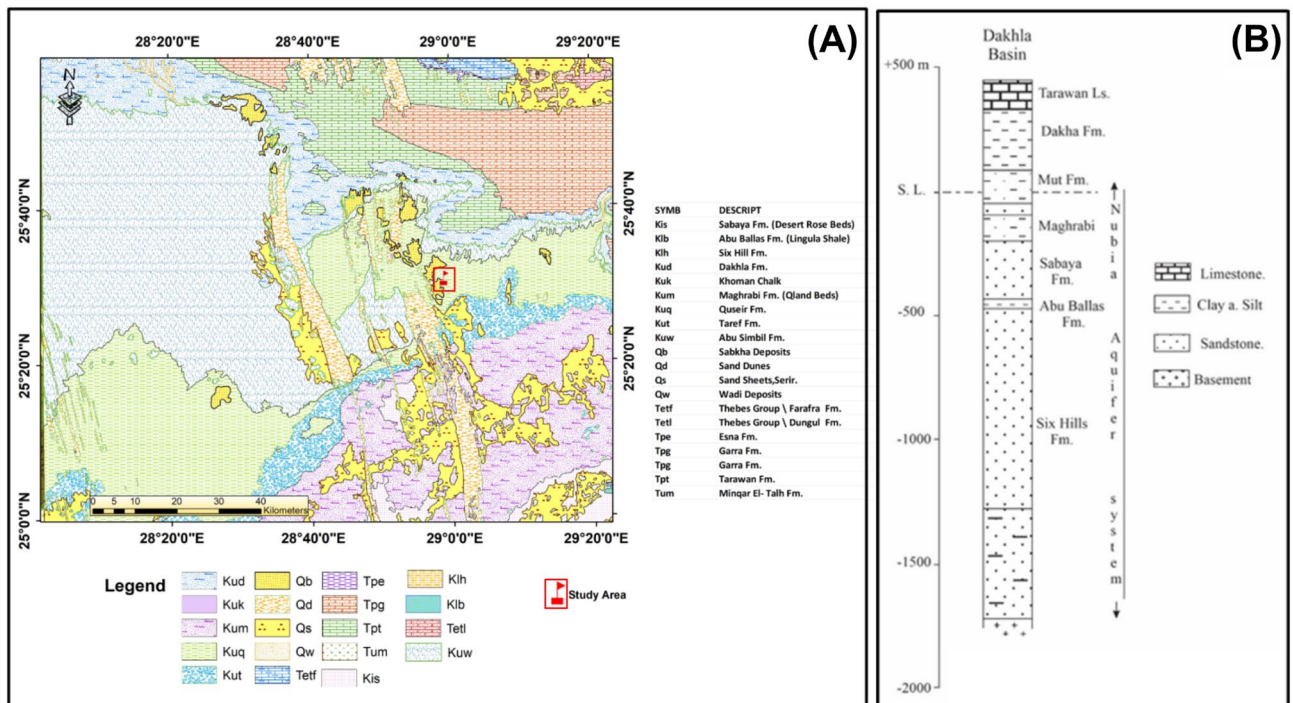


**Figure 2.** (A) Geological map of the Dakhla depression (after E.G.P.C. <sup>7</sup>). (B) Simplified geological section of the Dakhla Basin (after Said <sup>17</sup>).

and the sequence is Jurassic–Cretaceous in age. The layers are unconformably deposited on the Precambrian basement or, more locally, on Palaeozoic rocks in the west.

The study area's surface geology reveals many layers of the variegated shale that emerge on the surface and are covered in some places by layers of the Dakhla shale and in others by layers of the Tarawan Formation. Additionally, the region is defined by the existence of many fractures and warps in a variety of directions, the majority of which run northeast–southwest and perpendicular to it, i.e., northwest–southeast, which is consistent with similar patterns seen in other regions within the Western Desert <sup>20–22</sup>.

Before 1987, neither historical nor instrumental seismicity was recorded near the southwestern corner of the Western Desert. An earthquake with magnitude  $m_b = 5.3$  occurred on the El-Gilf El-Kebier Plateau on December 9, 1987. El-Baz et al. <sup>23</sup> investigated the geology of the region and found that it is influenced by two faults: the Gilf fault, which strikes N–S for 150 km within Egypt and continues southwards into Sudan, and the Kernal fault, which restricts the plateau's northwestern edge and strikes NW–SE. The Kemal fault crosses the northern end of the Gilf fault.

## Field surveys and data acquisition

### Geophysical surveys

In the area under investigation, field measurements were conducted using different geophysical tools, including land magnetic, seismic, TEM and VLF techniques. The magnetic total-field data were collected with a GSM-19 (Overhauser) and a base station for diurnal corrections. Continued measurements were acquired to cover the entire area around the smoke exit area (SEA). A comprehensive terrestrial magnetic survey was conducted in the Al-Hindaw region. Two Overhauser magnetometers were utilized: one was used as a stationary base station in various homogeneous locations, and the other was used for making observations approximately 0.5 to 1 m apart, depending on the walking speed. After correcting the data for diurnal and annual fluctuations, a map of the total magnetic field was created.

The TEM measurements were taken at ten points along the N–S profile that traverses the SEA. The distance between adjacent stations was between 100 and 200 m. The TEM data were acquired using a SIROTEM MK3 conductivity meter with a single loop design and a 50 m loop side length to reach a depth of approximately 150 m under the Earth's surface. The data were captured in composite mode using up to 30 discrete time intervals (time gates).

A total of 104 measurement points were observed along two lines utilizing the T-VLF device with an interval of 5 m between each station, as shown in Fig. 1. We used two transmitters with frequencies of 17,900 and 24,000 Hz. These transmitters give well-observed radio signals and portrayed a narrow azimuthal distribution. Typically, the tilt angle and ellipticity of the vertical magnetic polarization ellipse were deduced from the estimation of two orthogonal magnetic field components.

Additionally, three seismic shallow refraction profiles were acquired in a north–south direction, each of which had a length of 151 m with a total length of 453 m and passed by the SEA. Each line was shot many times in order to obtain good records, which allowed recording the largest possible time of arrival of seismic waves,

as well as obtaining a high-resolution model of the underlying structures in the research area. Six surface wave profiles were also recorded to obtain surface waves. The acquisition of surface waves was similar to the acquisition of traditional shallow seismic refraction profiles where the geophones are aligned in a straight line with equal geophone spacing. In the current study, a 48-channel seismograph and 4.5 Hz geophones were used. The geophone spacing that was used was 1 m. The roll-along acquisition technique was implemented, where only 24 channels were active during each shot. The shot was placed – 4 m from the first geophone. The shot process was shifted 4 m and repeated eight times. Figure 1 illustrates the locations of these profiles. In addition, two profiles of passive MASW were recorded using 48 geophones with 5-m intervals and a total length of 235 m to reach deeper parts. Finally, Microtremor measurements were acquired in the study area for 12 sites in a north–south direction with distances between 100 and 50 m. The data were recorded using Trillium 40 and Trillium 120 s seismometers (Nanometrics Inc.). The length of recording was approximately 2 h at each site.

In addition, continuous temperature logs were recorded using a GeoVista PT100 Sensor<sup>24</sup> in a downwards direction in two wells that are located close to the SEA. The probe that was used was designed to produce precise temperature readings in a borehole environment with a resolution of 0.01 °C.

## Geochemical surveys

### Rock sampling

Five different rock samples were collected from the research region (Fig. 1); four samples were taken from the SEA, and one sample was taken from an area that was 110 m to the northwest of the SEA. This location was once home to the same phenomena, but it no longer exists. During the process of collecting samples, extreme care was used to guarantee that they were not damaged by corrosion or by being burned. The samples were analysed on LECO SC 632 equipment at the Egyptian Petroleum Research Institute (EPRI), Cairo, Egypt, to measure their total organic carbon (TOC) and total sulfur (TS) concentrations following the procedure described by Prinz et al.<sup>25</sup>. The analysis consisted of burning nearly 100 mg of the powdered sample in the presence of oxygen, where the combustion temperature was increased gradually from 100 °C to more than 1000 °C. Moreover, X-ray fluorescence (XRF) measurements were conducted in EPRI on five powdered samples to obtain their elemental composition (major elements) using an Axios Sequential PANalytical 2005 WD\_XRF Spectrometer.

Organic petrography was performed on two samples with the highest TOC contents to qualitatively estimate the kerogen composition following the procedure described by Makled et al.<sup>26</sup>. For kerogen separation, 10 g of powdered sample was treated with HF and HCl acids, and the residues were screened via a 200- $\mu$ m brass sieve and then a 10- $\mu$ m nylon sieve. Moreover, the organic kerogen was separated from the residue using a solution of zinc chloride and then mounted on glass slides for microscopic analysis. Additionally, pyrolysis gas chromatography (Py-GC) analysis was conducted on the whole rock powder to examine the chemical composition of the organic kerogen. The obtained gas chromatograms often illustrate the major components within the organic kerogen and hence fingerprint the kerogen type, origin, and composition.

### Gas sampling

Seven locations in the research region were sampled for gas emissions using pre-empted 20 ml glass bottles and a silicone funnel linked to a silicon hosepipe. In the ISOLAB BV research laboratories in the Netherlands, gas chromatographic (GC) analyses were carried out to evaluate the molecular structure of the collected gases. The C<sub>1</sub>, O<sub>4</sub>, A<sub>1</sub>, and N<sub>2</sub> contents and their gas emissions were determined via a heated injection valve and a thermal conductivity detector (TCD) and an Agilent 6890 N/7890A/7890B GC (Agilent Technologies, Santa Clara, CA, USA) outfitted with a 12 m and 0.32 mm molsieve column (Agilent). The C<sub>2</sub><sup>+</sup>, CO<sub>2</sub>, and CO concentrations were evaluated utilizing an Agilent 6890 N/7890A/7890B GC outfitted with a heated injection valve, TCD, and FID, as well as a 50 m and 0.32 mm Porabond-Q column (Agilent). The readings were routinely calibrated using synthetic gas mixes with known compositions throughout the day. The O<sub>2</sub>, N<sub>2</sub>, and Ar gas readings were calibrated with atmospheric air. The detection thresholds for hydrocarbons are 1 ppm, whereas those for CO<sub>2</sub>, O<sub>2</sub>, and N are 100 ppm. The findings of compositional analyses of the examined Dakhla gas leaks were adjusted for air contamination by employing the (N<sub>2</sub>/O<sub>2</sub>) air and (Ar/O<sub>2</sub>) air values of 3.70 and 0.048, respectively, and the observed gases were given in mol%.

The carbon  $\delta^{13}\text{C}$  composition was measured for CO<sub>2</sub>, as well as the C<sub>1</sub>–C<sub>3</sub> hydrocarbon phases at the four sites that have the highest hydrocarbon gas contents, whereas the deuterium  $\delta_{\text{D}}$  of methane was measured for only one sample. In addition, nitrogen  $\delta^{15}\text{N}$  isotopic values were also measured for the same sites. At least three measurements were performed for each sample, and the average result was then reported. For  $\delta^{13}\text{C}$  isotope values in hydrocarbon phases, an Agilent 6890 N GC was connected to a Finnigan Delta S IRMS through a Finnigan GC-C II interface. For the determination of  $\delta^{13}\text{C}$  values in CO<sub>2</sub>, an Agilent 7890A GC interfaced to a MAT 253 IRMS through a GC-Isolink or Finnigan GC-C III interface was used. The values for carbon isotopes were provided with a maximum experimental error of (1 $\sigma$ ) of  $\pm 0.2\%$  compared to ‰VPDB. The deuterium values for methane were acquired using an Agilent 7890A GC coupled to a MAT 253 IRMS, and the  $\delta_{\text{D}}$  values were given relative to ‰VSMOW, with an experimental error (1 $\sigma$ ) of no more than  $\pm 5\%$ . Using an Agilent 7890A GC (interfaced to a Finnigan MAT 252 IRMS via a connected Finnigan GC-C II), the  $\delta^{15}\text{N}$  values for nitrogen in the examined gases were measured. The  $\delta^{15}\text{N}$  readings were routinely calibrated with nitrogen from ambient air, and the results were published with an experimental error (1 $\sigma$ ) of  $\pm 0.2\%$  relative to atmospheric N<sub>2</sub>.

## Methodology and results

### Geophysical data

#### Geomagnetic data

On the surveyed total magnetic intensity (TMI) map, the reduction to the pole (RTP) approach was employed to rectify the shift between sources and magnetic anomalies induced by the nonverticality of the normal field and magnetization. The inclination of the normal field was adjusted to 42.4 north, while the declination was set to 2.5 east<sup>27</sup>. The RTP terrestrial magnetic map of the AL-Hindaw region (Fig. 3A) shows that the majority of the anomalies are oriented NE–SW, NW–SE, and E–W. Positive magnetic anomalies are also visible in the eastern and northwest regions of the map, while negative anomalies are found in the centre. The tilt derivative magnetic anomaly map (Fig. 3B) clearly shows that the region is influenced by two fault systems, F1 and F2, which run NE and NW, respectively, and meet at the SEA.

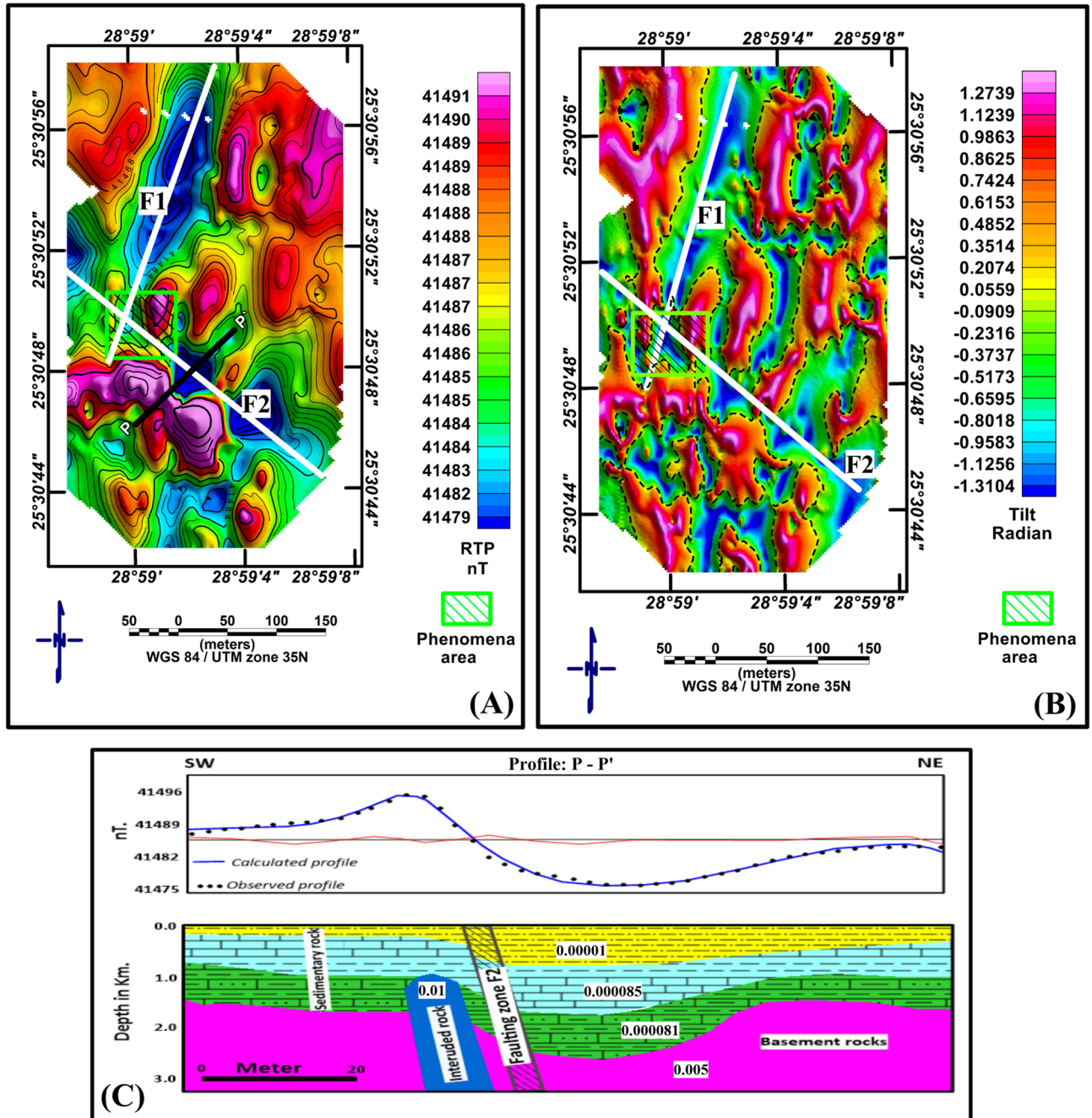


**Figure 3.** (A) RTP land magnetic map of the AL-Hindaw area. (B) Tilt derivative RTP magnetic anomaly map, where the yellow square delineates the SEA area. (C) 2D magnetic modelling along profile P-P'. The numbers in the modelled section refer to the magnetic susceptibility values in SI units.

Based on the theories of Talwani et al.<sup>28</sup>, a 2-D modelling approach was applied to selected profiles on the RTP map utilizing GMSYS-3D modelling software<sup>29</sup>. The 2D inversion model enables us to handle both layered structures and single objects, such as igneous intrusions. The approach is based on the correlation between the observed magnetic curve from the RTP magnetic map and the predicted curve. The magnetic susceptibility was the variable factor in the procedure that produced more or less full matching between the observed and computed curves. Within layers, magnetic susceptibility may vary both vertically and horizontally. Each causal body has a distinctive potential field that can be built by adjusting specific factors, including its extent, magnetic susceptibility, inclination, declination and x–z positions. On the basis of drilled wells and previously published depth estimations, we suggest that the sedimentary rock above the basement comprises three distinctive rock units. In the bottom layer, the two limestone rocks prevail, but in the upper layer, the shale deposit rocks predominate. By adjusting the magnetic susceptibility coefficients of the subsurface rocks and their accompanying intrusion as well as the depths of the basement layer, it is possible to match the estimated and observed magnetic curves, whereas the computed model's root mean square (RMS) value is 0.55. Figure 3C depicts the resulting model, in which it can be shown that fault structure F2 has been downthrown approximately 400 m.

#### Seismic data

**Shallow seismic refraction.** In this study, three shallow seismic refraction profiles were measured in the emission area. The data were processed, and a 2-D subsurface tomographic model of the study area was obtained from the arrival time inversion. The processing was performed first using the initial model obtained by the time-term inversion technique, which was the input for the tomographic inversion using SeisImager software. All interpretation theory and practice methods are summarized in Geometrics and OYO SeisImager/2D™ manual, 2009 Ver. 3.3<sup>30</sup>. Figure 4 provides examples of a stratified model determined by time-term inversion (initial model) and tomography inverted model (second step). The third profile barely passed over the emission area location. The obtained model shows that the study area comprises four layers with P-wave velocities between 300 m/sec and 1890 m/sec. The obtained model shows that the surface layer is removed at the emission site, and two faults might bind the emission site.

**Multichannel analysis of surface waves (MASW).** The MASW method<sup>31–34</sup> is a widely used approach for imaging subsurface structures<sup>35</sup>. The analysis of the acquired waveforms depends on measuring the dispersion of the recorded Rayleigh waves. Six MASW profiles were measured in the SEA, as shown in Fig. 1.

The processing of the acquired profiles was performed using a genetic algorithm. This algorithm has several advantages over traditional processing procedures<sup>36</sup>. Figure 5B shows an example of the obtained curves. A 1-D subsurface model was obtained for each shot (Fig. 5C), and then a 2-D subsurface model was obtained. Figure 5D shows a merging of three MASW profiles passing beside the emission site. The processed shear wave velocity model shows that the area comprises four strata with shear wave velocities ranging from 100 to 333 m/sec. The disappearance of the surface layer at the emission location and the faulting impacting the region are both visible in the 2-D profile.

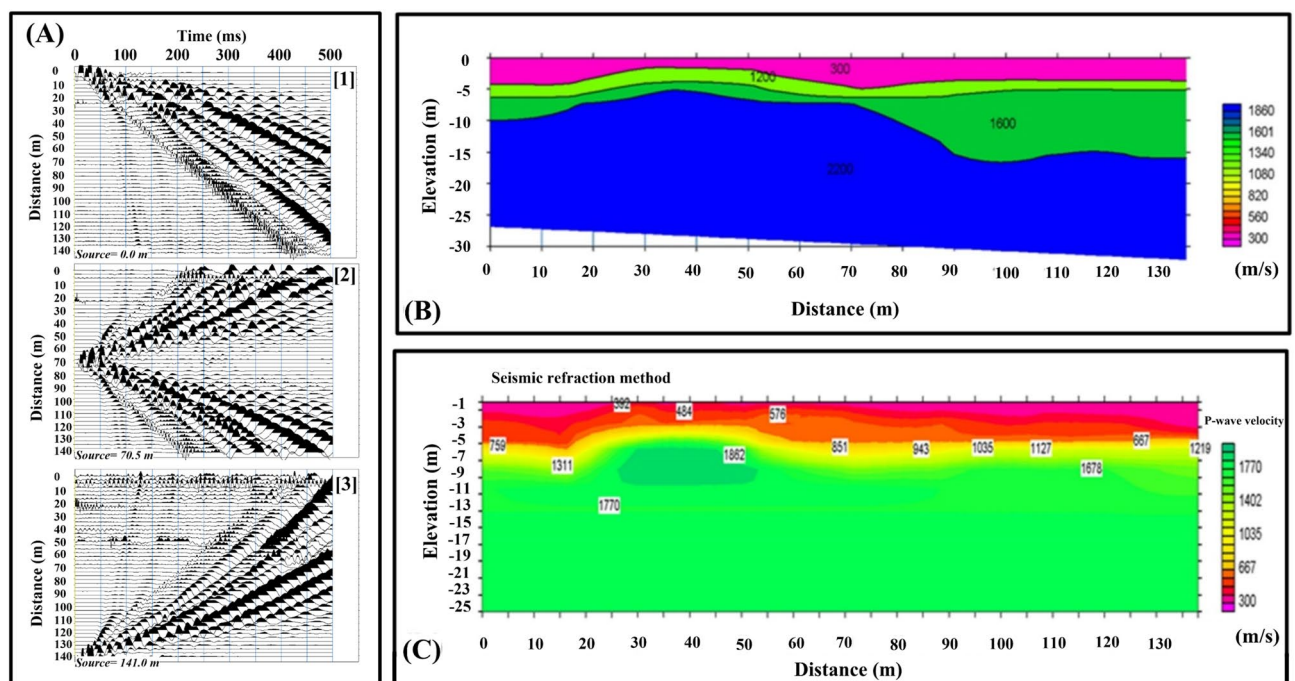


**Figure 4.** (A) Examples of the obtained seismic records, (A-1) Normal shot, (A-2) Mid shot and (A-3) reverse shot; (B) Stratified model determined by time-term inversion (initial model); (C) the obtained seismic tomographic inverted model of the emission area.

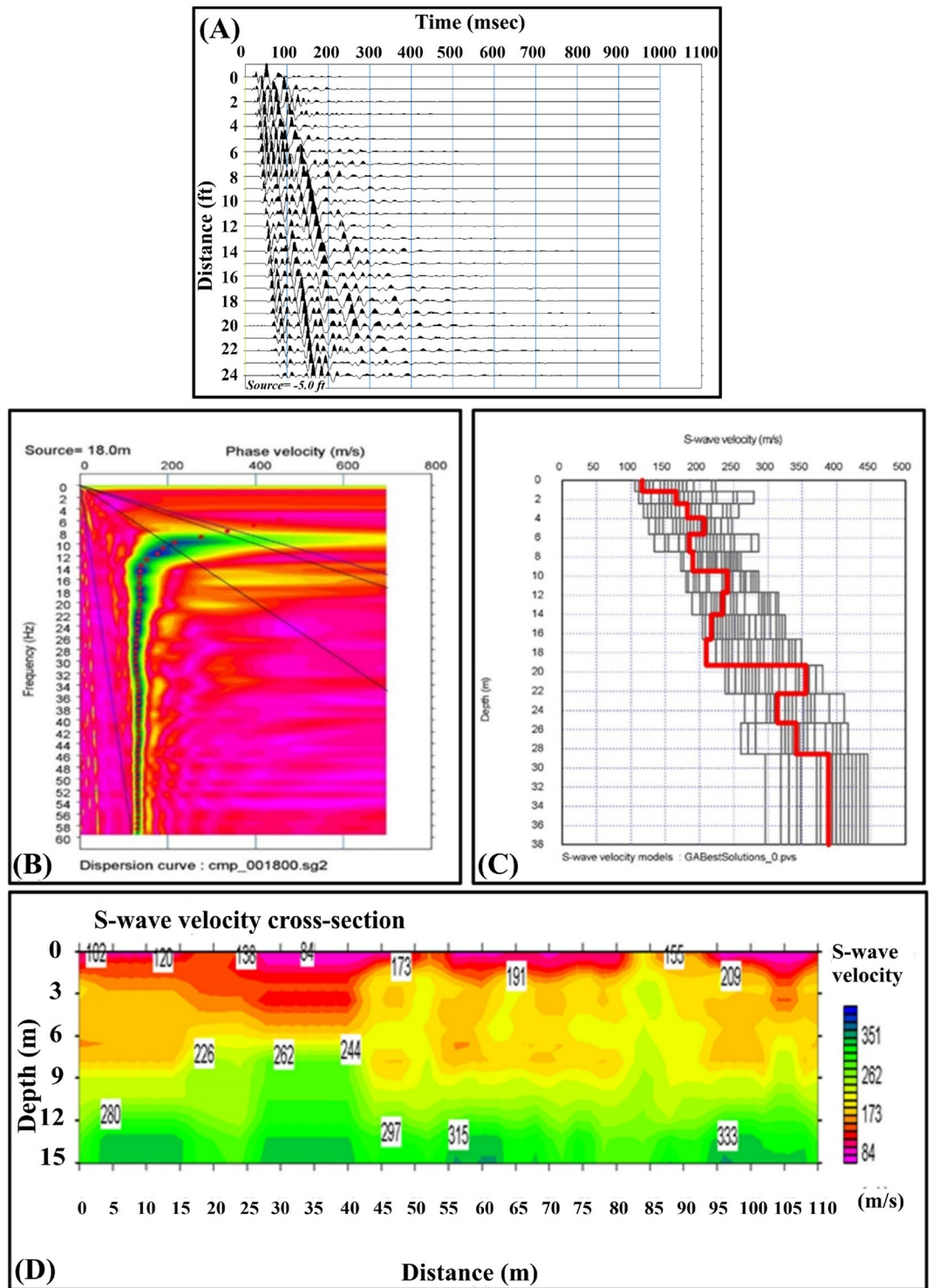


**Figure 5.** (A) Example of the obtained seismogram; (B) Example of the obtained dispersion curves; (C) example of the obtained 1-D model; (D) the obtained 2-D shear wave velocity model.

**Passive MASW.** This method has been used many times worldwide by many scholars <sup>32,37–39</sup>. Two passive MASW profiles are acquired at the site. An example of the obtained dispersion curves is shown in Fig. 6B. For deeper subsurface imaging, the acquired dispersion curves are combined with those from the MASW. The merged curves are illustrated in Fig. 6B. Figure 6D demonstrates the shear wave subsurface model of the study site utilizing both the dispersion curves obtained from MASW and passive MASW. The last figure indicates much heterogeneity appearing close to the surface compared to the deeper part of the merged section. Figure 4 shows that the P-wave velocities in the study area are 300 m/sec, 1200 m/sec, 1600 m/sec and 2200 m/sec for

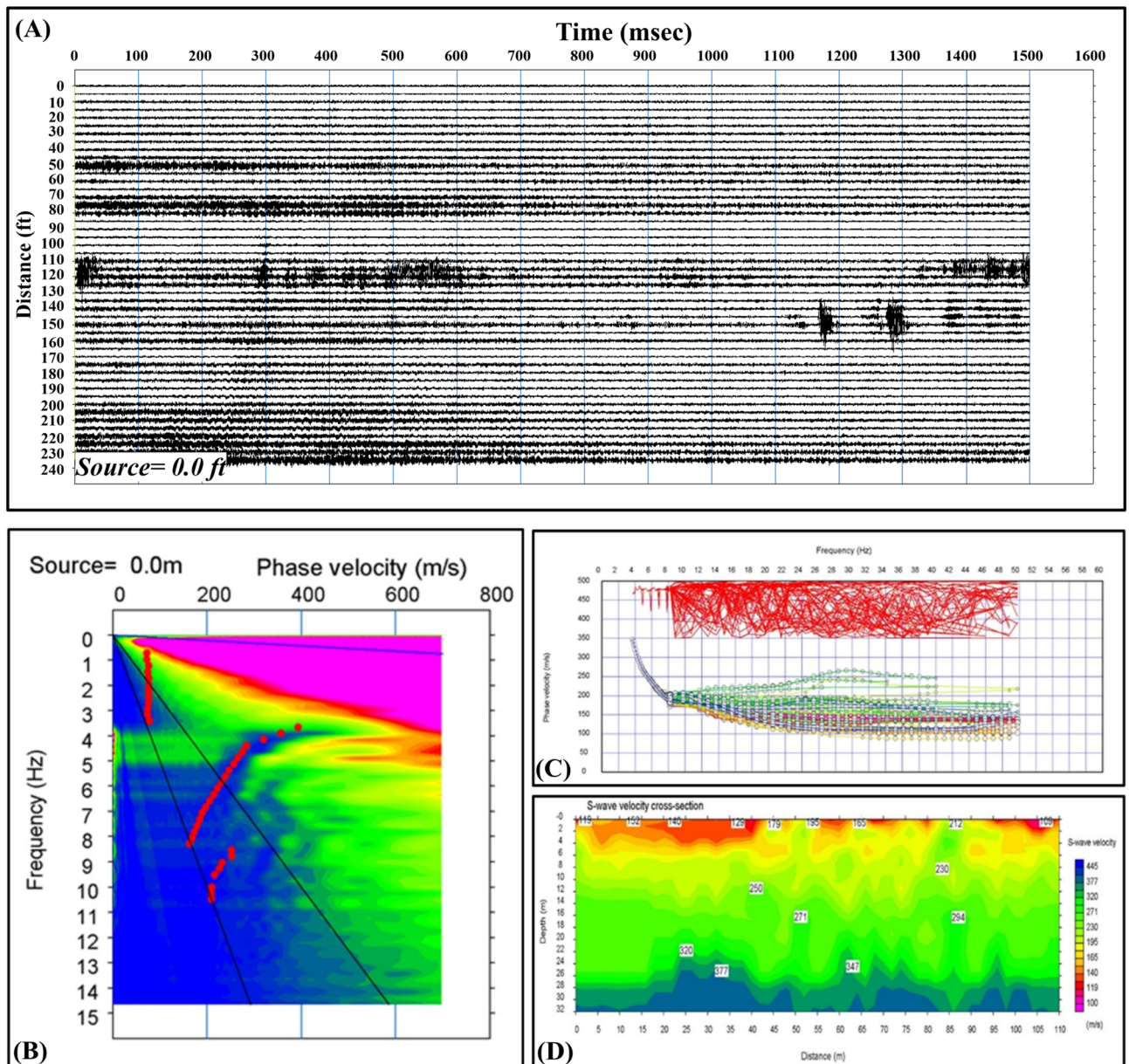


**Figure 6.** (A) Example of the obtained passive seismogram; (B) Illustration of a dispersion curve produced from passive MASW measurements; (C) example of the merged dispersion curve generated from active and passive MASW; and (D) the subsurface model derived by integrating the active and passive MASW profiles.

the geoseismic layers 1, 2, 3, and 4. On the other hand, Fig. 5 shows a shear wave velocity profile, where the shear wave velocity is 150 m/sec in the first layer, 200 m/sec in the second layer and 350 in the third layer. The obtained  $V_p/V_s$  in the study area ranges between 2.0 and 4.0. These high values of the  $V_p/V_s$  can be attributed to the gas occurrence and associated high temperature.

**Microtremor analysis.** The seismic noise measurements were acquired close to the emissions at 12 sites with interstation distances of 10 and 20 m, as shown in Fig. 1. The aim of these measurements was mapping the variation in the dominant frequency ( $F_0$ ) using the HVSR technique<sup>40</sup>, where the change in the value of  $F_0$  reflects the difference in the subsurface structures<sup>41–43</sup>. The data were analysed using Geopsy<sup>44</sup>. Figure 7A shows the analysis applied to the acquired data.

The analysed data show that the  $F_0$  values within the study area range between 0.78 and 1.93 Hz, with a sharp change in  $F_0$  values between stations ST03 and ST04 and ST09 and ST10 (Fig. 7B). Usually, these differences may be attributed to faulting.

**Local seismic network.** A temporary network of 4 broadband seismometers was installed with the other Egyptian National Seismological Network (ENSN) stations near the study area (Fig. 1). Establishing such networks aims to monitor microearthquakes, which may be associated with this phenomenon. The network was operated

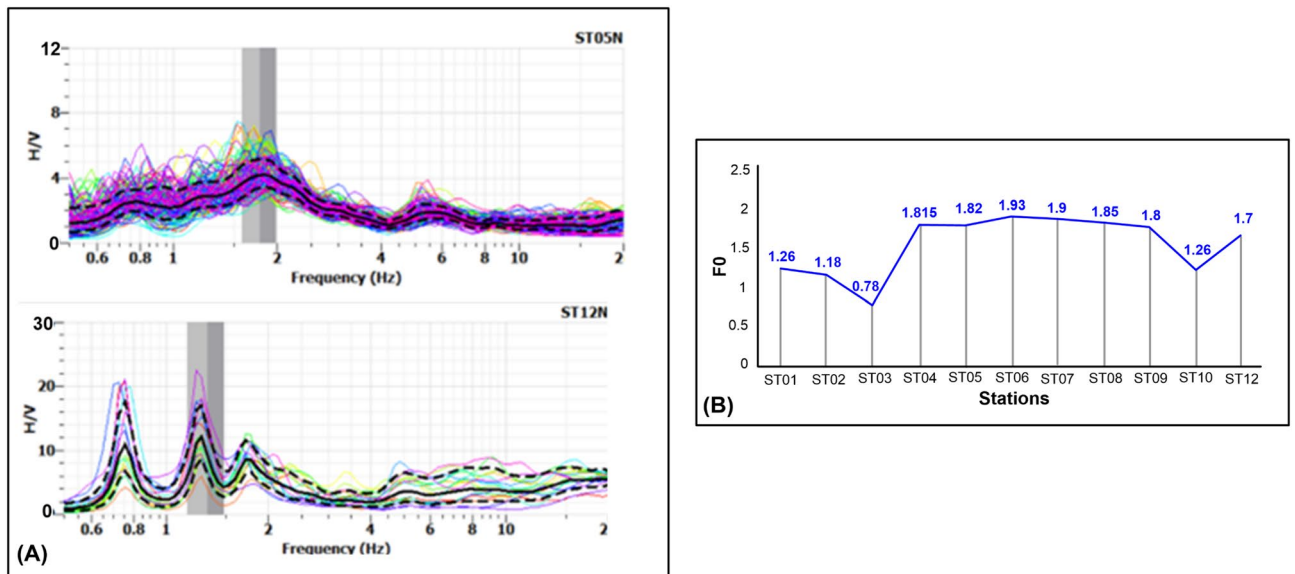


**Figure 7.** (A) The examination of microtremor data from sites 5 and 12. (B) The spatial distribution of the obtained  $F_0$  values.

for 2 weeks during and after the emission. During the installation of these stations, no seismic activity was recorded, which could be related to the phenomenon being investigated.

*TEM data*

Using the ZONDTEM1D program<sup>45</sup>, analyses and modelling of TEM data were performed. A range of criteria, including the number of layers and their thicknesses, were evaluated to determine the best possible starting model for TEM data processing. The robust model is the model with the least amount of error, the best fit, and the greatest compatibility with the given geological data. The procedure was carried out in a refined manner until a composite model satisfying the TEM data was produced. Each model characterizes the geoelectrical properties of the underlying layer at its corresponding location. The obtained models have been utilized for generating a north–south geoelectrical cross-section, as shown in Fig. 1. The geoelectrical section constructed in the study region is illustrated in Fig. 8.

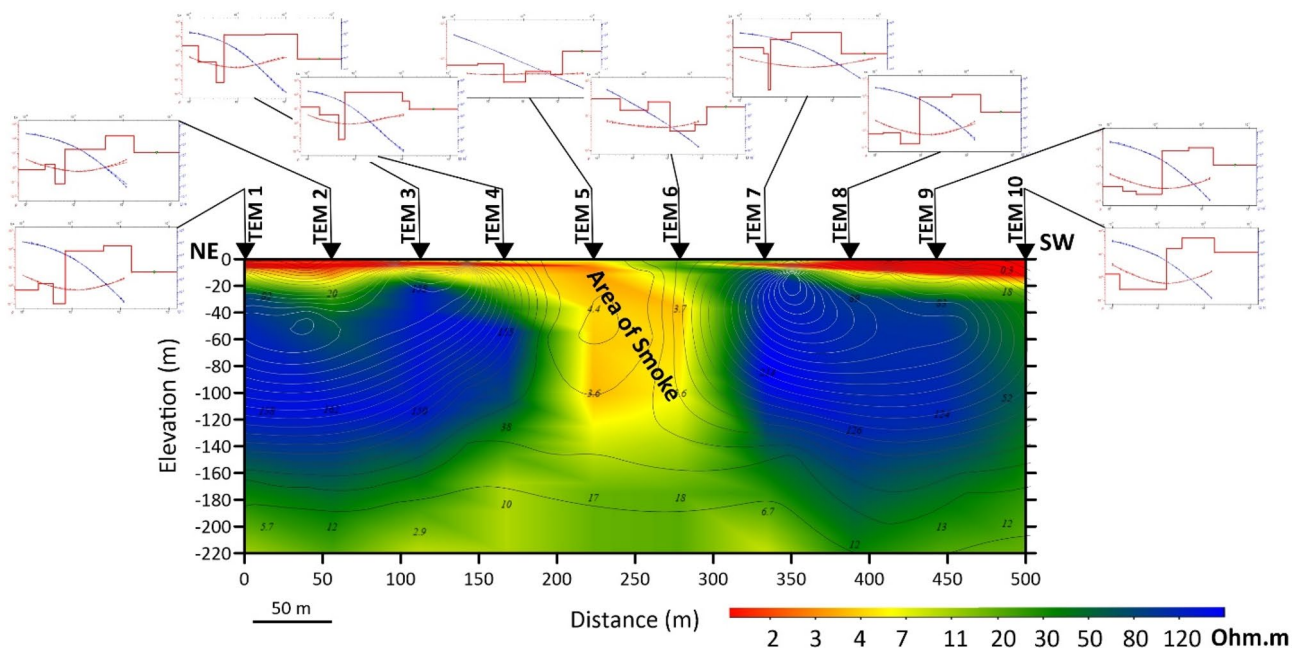


**Figure 8.** Geoelectrical cross-section of the TEM data along the profile passing through the smoke exit area (SEA). The locations of the TEM soundings are shown in Fig. 1. The above graphs refer to the results of 1-D modelling of TEM data.

The geo-electrical cross-section shows that the area where smoke and high temperatures appear is characterized by a decrease in electrical resistivity compared to the rest of the areas, which indicates the effect of high temperatures on electrical conductivity, leading to its warming up and thus a reduction in electrical resistance.

#### VLF data

The processing of the VLF data aims to calculate the subsurface current density distribution. The data are processed using the VLF2DMF program<sup>46</sup> to calculate the K-H filter, and then inverse modelling is applied to estimate the subsurface resistivity distribution. As illustrated in Fig. 1, the first profile extends from north to south, while the second profile extends from northeast to southwest. Both profiles intersect the SEA. The K-H filter<sup>47</sup> in both profiles demonstrates a significant amount of variance in the real component amplitude in excess of the SEA. In addition, the resistivity model demonstrates a very low resistivity anomaly beneath the smoke area. The VLF data lend credence to the conclusion drawn from the TEM data, which is that an increase in the rock temperature results in an increase in the rock electrical conductivity (Fig. 9).

#### Temperature logs

Temperature logs are able to provide information on the change in temperature as the probe traverses deeper, and as a result, the temperature gradient in the measured well can be determined. The log recording in well Mut 14, located 1300 m south of the SEA, attained a maximum depth of 112 m. At this depth, a temperature reading of 37 °C was recorded. On the other hand, the log recording in well Hindaw 5, which is situated 2150 m north of the SEA, reached a maximum depth of 38 m. A temperature measurement of 36 °C was made at this depth (Fig. 10). The trend of the temperature curves in both wells demonstrates that there is no discernible change in temperature with depth, which implies a low temperature gradient (approximately 0.025 °C/m in well Hindaw 5 and 0.022 °C/m in Mut 14).

#### Geochemical data

##### Elemental analysis

Data from elemental geochemical analyses of the five obtained rock samples are shown in Table 1. The ranges of TOC and TS values in the samples are between 0.05 and 4.29 wt% and 0.09 and 12.6 wt%, respectively. The

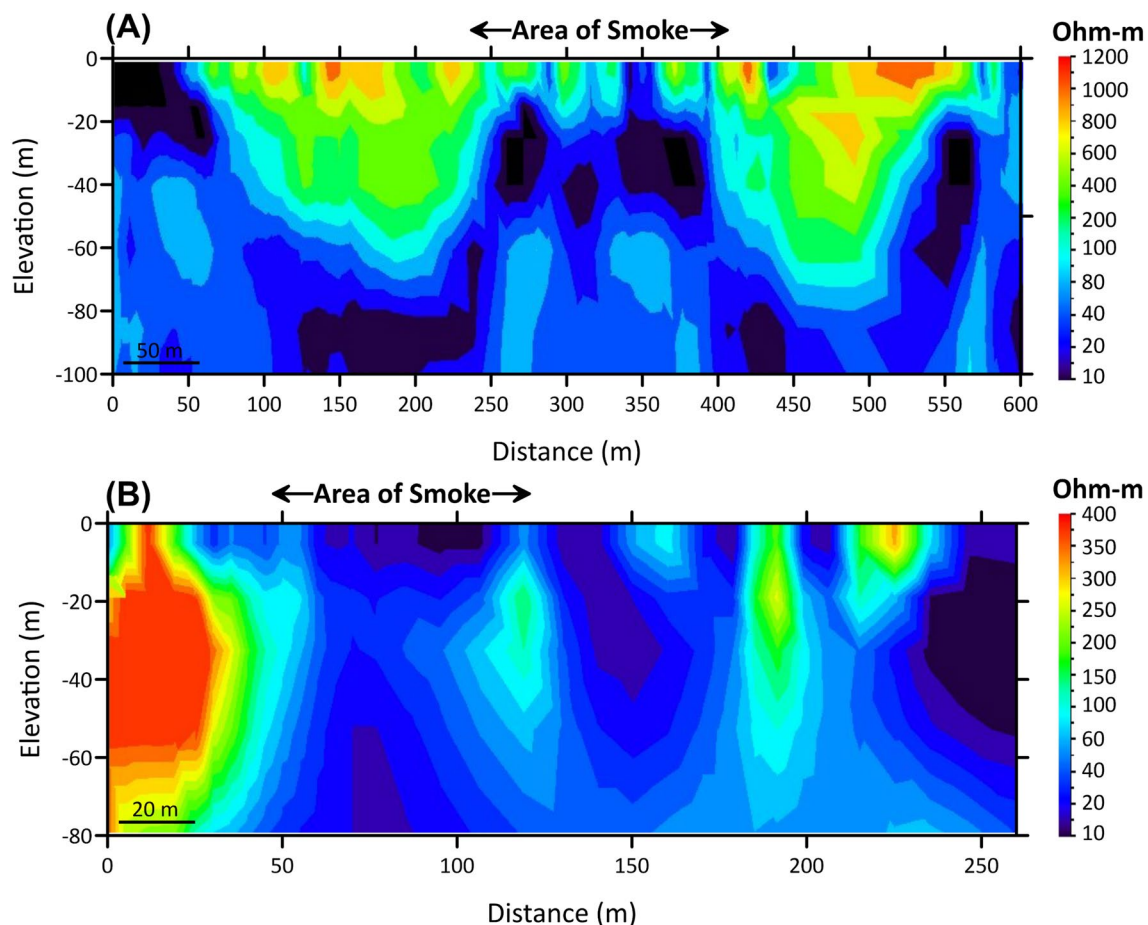


**Figure 9.** Modelled resistivity cross-sections of the VLF data along (A) profile 1 and (B) profile 2, both of which pass through the SEA.

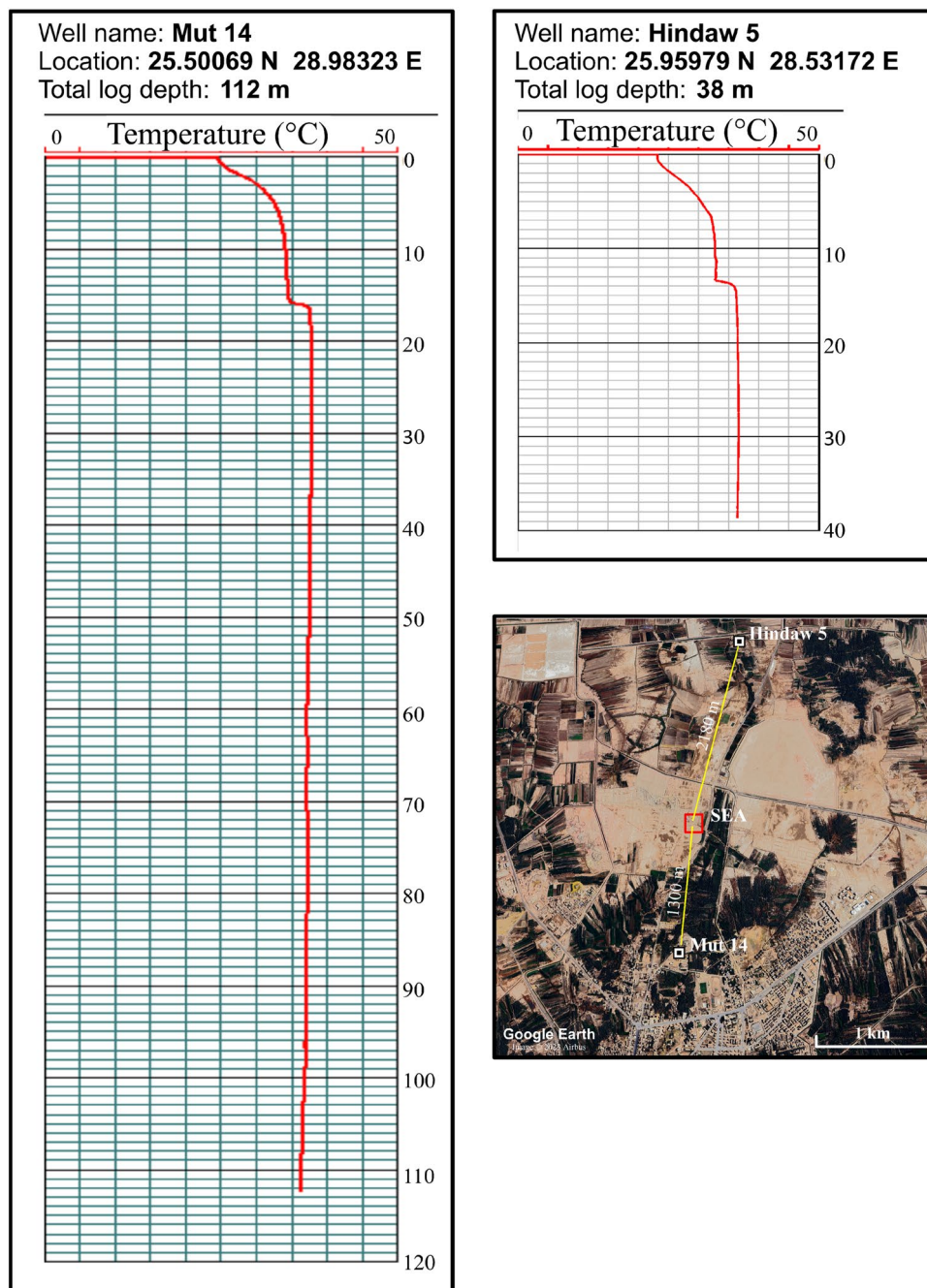


**Figure 10.** Temperature recording using the GeoVista well logging instrument in two water wells near the SEA. The Google Earth map shows the location of these wells from the area of smoke.

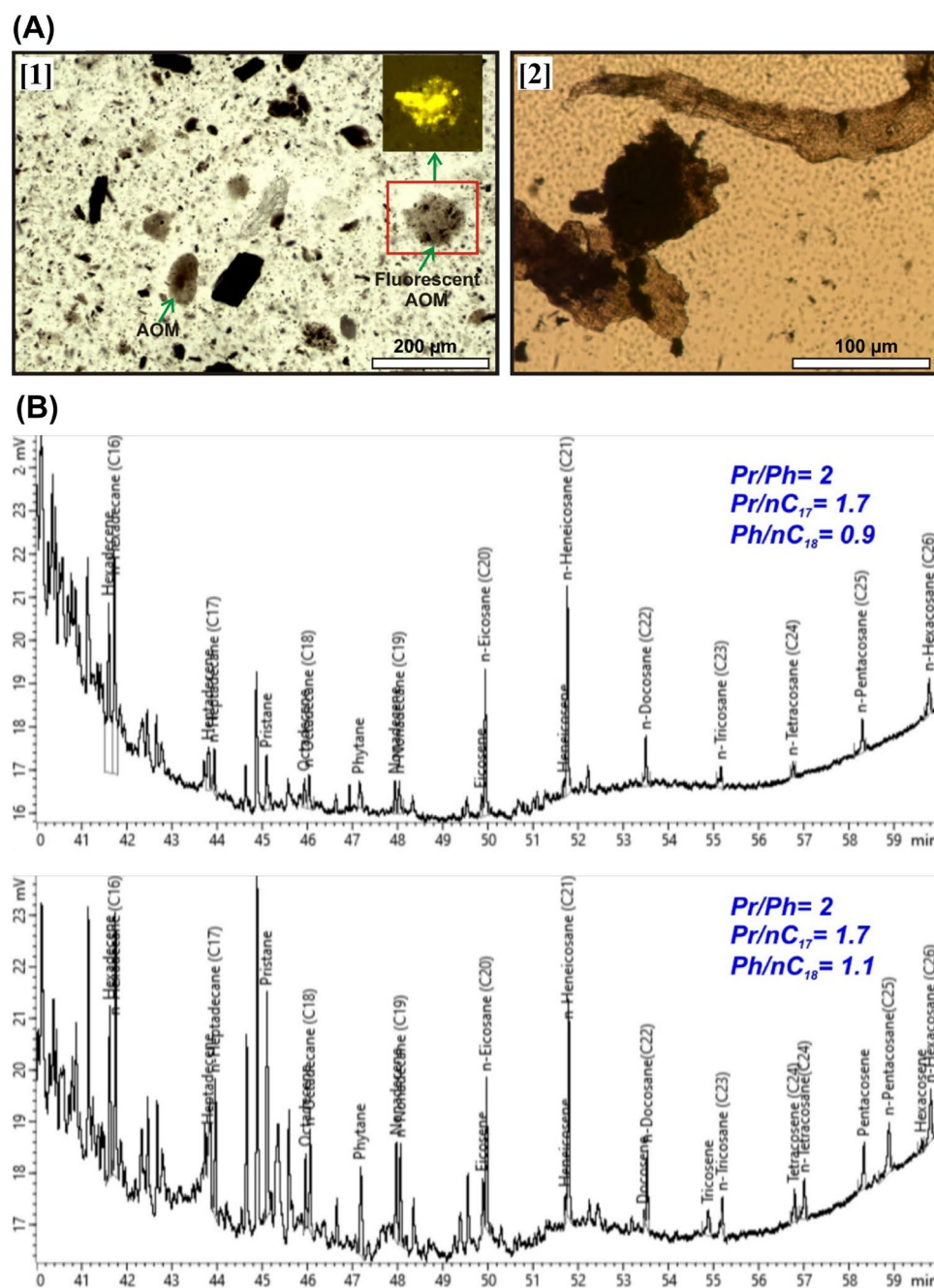
Sample	TOC	Na <sub>2</sub> O	MgO	Al <sub>2</sub> O <sub>3</sub>	TiO <sub>2</sub>	K <sub>2</sub> O	Fe <sub>2</sub> O <sub>3</sub>	CaO	MnO	TS	SiO <sub>2</sub>	P <sub>2</sub> O <sub>5</sub>
S <sub>1</sub>	0.06	0.193	1.27	14.9	0.77	1.82	12.8	1.22	0.059	0.3	61	1.17
S <sub>2</sub>	0.27	0.08	1.76	19.1	1.07	2.25	5.75	0.481	0.05	1.29	58.3	0.28
S <sub>3</sub>	0.05	0.09	3.75	15.4	1.09	3.38	9.74	3.11	0.16	0.09	51.9	1.84
S <sub>4</sub>	0.71	0.12	1.3	17.4	1.69	2.79	11.1	0.55	0.04	0.62	51.1	0.12
S <sub>5</sub>	4.29	0.46	1.25	7.85	0.44	0.99	26.9	1.43	0.24	12.6	19	0.32

**Table 1.** Elemental composition of the studied Dakhla shale samples.

shales are enriched in  $\text{Al}_2\text{O}_3$  (7.85–19.1 wt%),  $\text{SiO}_2$  (19–61 wt%), and  $\text{Fe}_2\text{O}_3$  (5.75–26.5%), whereas all other oxides have reported values less than 5%. Notably, the shales are highly depleted in  $\text{Na}_2\text{O}$ , with values in the range of 0.08–0.46 wt%. Similarly, the shales contain traces of  $\text{MnO}$  (0.05–0.24 wt%), whereas the concentrations of  $\text{CaO}$  and  $\text{MgO}$  are variable and range from 0.48 to 3.11 wt% and 1.25 to 3.75%, respectively. Furthermore, the contents of  $\text{P}_2\text{O}_5$  vary in a wide range from 0.12–1.84 wt%.

#### Organic petrography

The analysed samples ( $S_4$ ,  $S_5$ ) with the highest TOC values are less degraded and contain well-preserved organic matter. Fine-grained fluorescent and nonfluorescent diffuse brown and opaque amorphous organic materials (Fig. 11A[1]) and fluorescent cuticles (Fig. 11A[2]) are the most abundant components. The terrigenous organic matter is represented by lath-shaped translucent brown phytoclasts. Palynomorphs and vitrinite fragments are absent. The preserved organic matter points to abundant type II and blended type II/III kerogen.



### Molecular composition of bitumen extracts

Extracted bitumen from the S<sub>4</sub> and S<sub>5</sub> samples displays relative enrichment in n-alkanes in the range of C<sub>1</sub>–nC<sub>15</sub> (>90%). Alkanes (~60%) and aromatics (~20%) are the most abundant components, whereas isoparaffins (~6%) and naphthalenes (~5%) are comparatively less abundant (Table 2). The samples have similar isoprenoid pristane/phytane Pr/Ph and isoprenoid/n-alkane (Pr/nC<sub>17</sub>, Ph/nC<sub>18</sub>) values (Fig. 11B).

### Gas chemistry

The primary phases shown in the examined gas manifestations are gaseous N<sub>2</sub>, CO<sub>2</sub>, Ar, CO, and CH<sub>4</sub> (Table 3). N<sub>2</sub> is the most abundant gas phase, varying in a narrow range from 86.32 to 88.53 vol%. CO<sub>2</sub> is the second most abundant gas phase, with a narrow range of concentrations from 10.27 to 11.23 vol%. Argon is present in significant concentrations from 1 to 2.28%. Traces of CO are recorded from 0.09 to 0.15 vol%.

Hydrocarbon gases are mainly represented by methane (0.025–0.41 vol%), ethane (0.001–0.064 vol%), and propane, with a maximum recorded value of 0.04 vol%, and the C<sub>6</sub>+ components vary from 0.01 to 0.14 vol%. The δ<sup>13</sup>C<sub>CO<sub>2</sub></sub> values vary in a wide range between –25.5 and –13.9‰ (Fig. 12). The δ<sup>13</sup>C rates of methane, ethane and propane are quite identical and heavier than –30‰ and display offsets of less than 3‰. The δD of methane was measured at one site, revealing a value of –160‰. Moreover, the δ<sup>15</sup>N values of the nitrogen gases are quite negative in the range of –0.1 to –0.4‰.

The isotopic composition of the different gas phases often points to their origin and mechanism of generation (6,10,48–52 and references therein). The measured δ<sup>13</sup>C<sub>CO<sub>2</sub></sub> values point to the organic origin of the CO<sub>2</sub> gases due to the thermal decomposition of organic-rich sediments (Fig. 12A). Light δ<sup>13</sup>C<sub>CO<sub>2</sub></sub> values <–13‰ reveal minimal

Sample	C <sub>1</sub> –C <sub>5</sub> %	nC <sub>6</sub> –C <sub>14</sub> %	nC <sub>15+</sub> %	Pr/Ph	Pr/nC <sub>17</sub>	Ph/nC <sub>18</sub>
S <sub>4</sub>	54	38	8	2	1.7	0.9
S <sub>5</sub>	58	36	15	2	1.7	1.1

**Table 2.** Geochemical characteristics of the bitumen extracted from the Dakhla organic-rich shales.

Site	C <sub>1</sub>	C <sub>2</sub>	C <sub>3</sub>	C <sub>6+</sub>	N <sub>2</sub>	CO <sub>2</sub>	CO	Ar	δ <sup>13</sup> C <sub>CO<sub>2</sub></sub>	δ <sup>13</sup> C <sub>Cl</sub>	δD <sub>Cl</sub>	δ <sup>13</sup> C <sub>C<sub>2</sub></sub>	δ <sup>13</sup> C <sub>C<sub>3</sub></sub>	δ <sup>15</sup> N
1	0.03	0.00	0.00	0.03	87.83	10.85	0.15	1.10	–	–	–	–	–	–
2	0.03	0.00	0.00	0.01	88.53	10.27	0.09	1.07	–25.5	–29.6	–	–28.9	–	–0.1
3	0.06	0.00	0.00	0.02	87.24	11.45	0.14	1.09	–	–	–	–	–	–
4	0.06	0.00	0.00	0.01	87.46	11.23	0.16	1.08	–25.4	–24.8	–	–25.5	–27.2	–0.2
5	0.06	0.00	0.00	0.02	87.36	11.37	0.14	1.05	–	–	–	–	–	–
6	0.06	0.00	0.00	0.01	86.32	11.18	0.14	2.28	–25.4	–24.2	–	–25.3	–26.5	–0.4
7	0.41	0.06	0.05	0.14	87.25	11.06	0.00	1.00	–13.9	–24.1	–160	–	–	–0.5

**Table 3.** An analysis of the chemical and isotopic contents of gas seeps from seven locations throughout the research region.

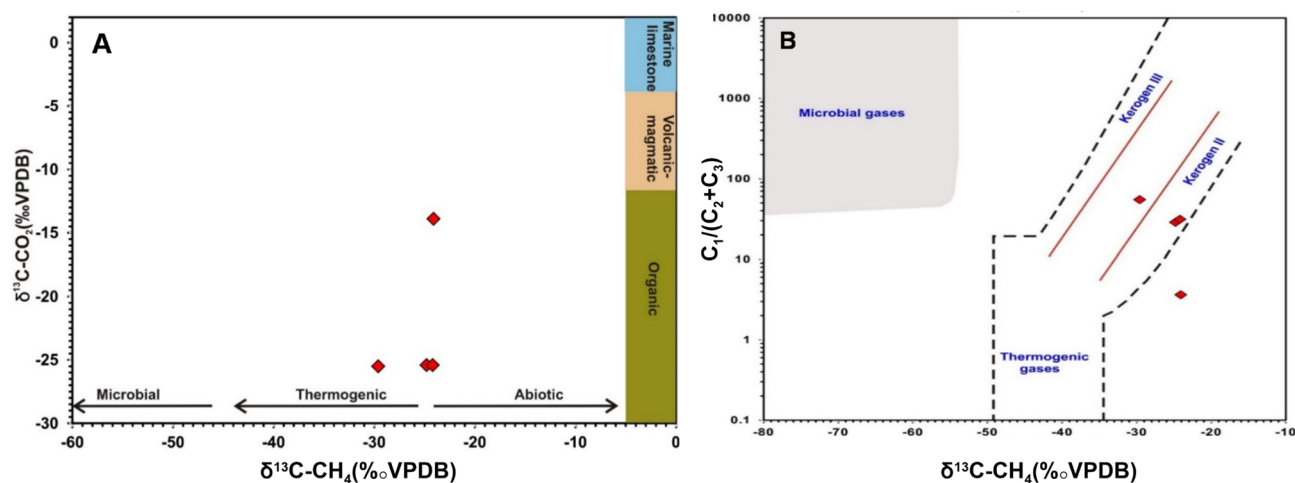


**Figure 12.** (A) δ<sup>13</sup>C<sub>CH<sub>4</sub></sub> versus δ<sup>13</sup>C<sub>CO<sub>2</sub></sub> cross-plot illustrating the organic origins of both CO<sub>2</sub> and CH<sub>4</sub> gases; (B) δ<sup>13</sup>C<sub>CH<sub>4</sub></sub> versus the molecular C<sub>1</sub>/(C<sub>2</sub> + C<sub>3</sub>) ratio showing that the vast majority of the gas samples are grouped together in the organic thermogenic zone of Bernard et al., 1978<sup>48</sup>.

or no contribution from either volcanic or magmatic  $\text{CO}_2$ , and light negative values preclude any input from the thermal decomposition of carbonate-rich sediments<sup>5,6</sup>. Similarly, the molecular versus isotopic composition of the hydrocarbon gas phases typifies a pure thermogenic origin of the hydrocarbon gases (Fig. 12B). This is further confirmed by the relatively wet composition of the hydrocarbon gases ( $\text{C}_1/\text{C}_2 + \text{C}_3 < 100$ ), as well as the elevated concentration of the  $\text{C}_{6+}$  hydrocarbons. The relatively heavy  $\delta^{13}\text{C}_{\text{CH}_4}$  values coupled with low molecular ratios support hydrocarbon gas formation via thermal cracking of sediments enriched in type II kerogen capable of generating wet-type gases<sup>53</sup>. Furthermore, the  $\delta^{13}\text{C}_{\text{CH}_4}$  and  $\delta\text{D}_{\text{CH}_4}$  plot correlates with gases generated by geothermal thermogenic processes (Fig. 13A). Additionally, the isotopic values of ethane and propane that do not correlate with those derived from oil cracking (oil-type gas) support their derivation from thermal cracking of the kerogen (Fig. 13B).

## Integrated results and discussion

Geomagnetic measurements indicated the existence of a closed anomaly with high values near the smoke exit area (SEA), shown as a yellow square in Fig. 3, that quickly declines to the northeast, which is linked to the presence of a fault. This result indicates that this fault's linear anomaly runs northwest–southeast and connects with another primary fault (running northeast–southwest) in the smoke exit area. The results of the VLF, as well as the results of the TEM, revealed that the area of smoke and high temperatures is characterized by a decrease in electrical resistivity compared to the rest of the areas, indicating that high temperature has an effect on electrical conductivity, causing it to increase and, as a result, reduce the electrical resistivity in the area of smoke and high temperatures. This process relies on the fact that the electric resistivity of aqueous solutions in the interstitial spaces in the rocks decreases with increasing temperature. This is because a decrease in the viscosity of water increases the mobility of ions<sup>54</sup>.

Using geophysical data, it was discovered that the study area is exposed to two main faults and that the smoke exit area is located at the intersection of these two faults. It was also discovered that the study area contains numerous cracks and fissures, which could have been caused by high temperatures. These faults and fractures act as routes and outlets for the rising of groundwater from aquifers; the groundwater that has risen aids in the reaction processes occurring in the smoke-bearing region inside the fault zone.

The temperature records obtained from the two wells adjacent to the research region exhibit typical temperature gradients that align with the range observed and computed in other studies conducted in the Western Desert<sup>22,55,56</sup>. Since these wells draw water from the shallow aquifer at a depth of approximately 300 m, they indicate that the groundwater is unaffected by the high temperature caused by the phenomenon under study and that this phenomenon occurs close to the Earth's surface.

In terms of geochemistry, the studied gas seeps have been generated via near-surface reactions coupled with thermal degradation of materials rich in type II and II/III kerogen in Mut shales. Petrological data reveal abundant cuticles and amorphous organic matter in the fresh samples, typifying their ability to generate wet gases upon thermal maturation<sup>57–59</sup>. Additionally, the TOC and TS contents reveal that the studied organic-rich shales were deposited under anoxic bottom water, resulting in good preservation of the organic matter. (Fig. 14A). Sulfur was preferentially bound to the organic matter rather than reactive iron (Fig. 14B), resulting in the generation of sulfur-rich kerogen (type II S), typifying the assemblage of organic material in aerobic conditions in the presence of sulfate-reducing bacteria<sup>60,61</sup>.

The composition of bitumen extracts confirms the deposition of organic matter in a reducing environment (Fig. 15A). High-temperature catagenetic degradation of sulfur-rich kerogen would generate mainly  $\text{CO}_2$  and hydrocarbon gases in the range of  $\text{C}_1$ – $\text{C}_5$  coupled with the release of sulfur-rich compounds<sup>62,63</sup>. Indeed, the chemistry of the studied gases and the precipitation of sulfur in the vicinity of the gas seeps are consistent with the hypothesis of gas generation via catagenetic cracking of sulfur-rich kerogen in the Mut shales.

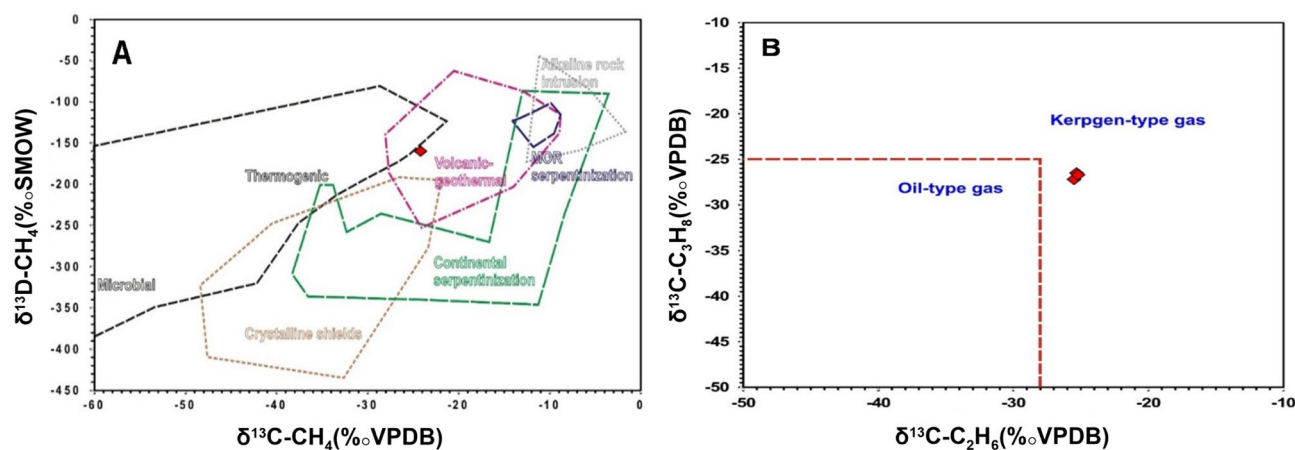


**Figure 13.** (A) The  $\delta\text{D}_{\text{CH}_4}$  and  $\delta^{13}\text{C}_{\text{CH}_4}$  gas origin diagram of<sup>10</sup>, illustrating the mixed thermogenic volcanic–geothermal source of  $\text{CH}_4$  in the investigated gas seeps; (B)  $\delta^{13}\text{C}_{\text{C}_2\text{H}_6}$  versus  $\delta^{13}\text{C}_{\text{C}_3\text{H}_8}$  cross-plot, showing that the  $\text{C}_2 + \text{C}_3$  phases in the gas seeps were formed via thermogenic cracking of the kerogen.

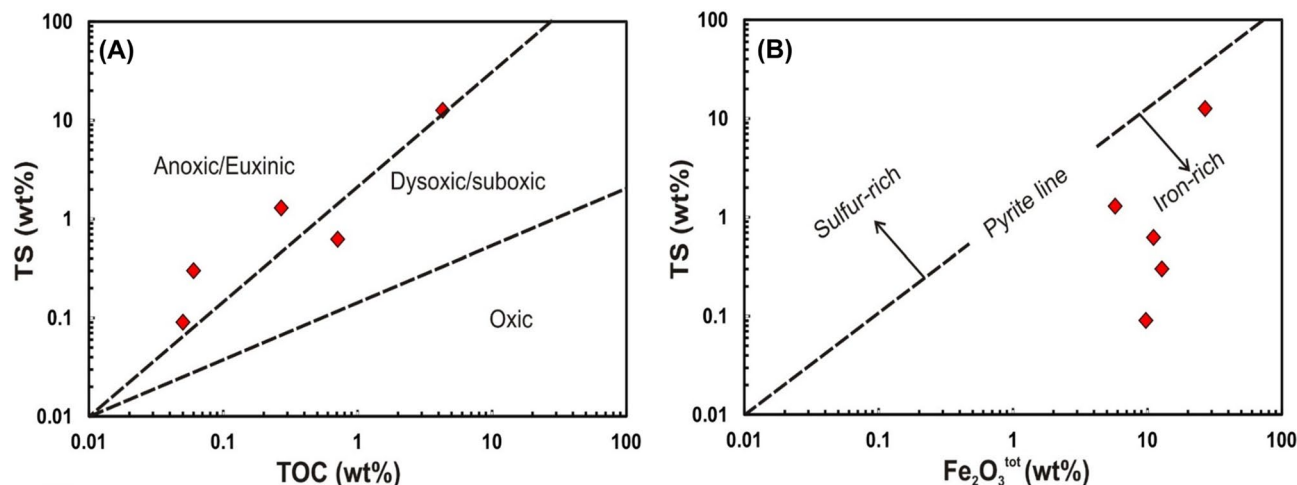


**Figure 14.** Total sulfur (TS) versus TOC (A) and total iron as  $\text{Fe}_2\text{O}_3$  (B) for the studied Dakhla shale samples illustrate their iron-rich composition and deposition in an anoxic–suboxic depositional environment.

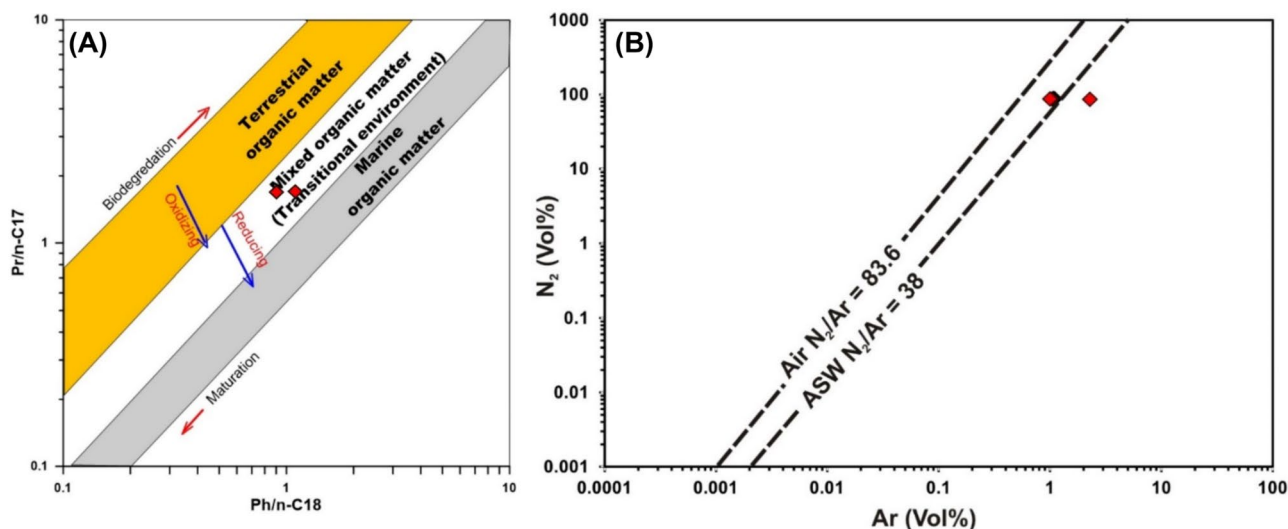


**Figure 15.** (A) Isoprenoid/n-alkane diagram of Shanmugam (1985)<sup>64</sup> confirming the reducing depositional environment of the Dakhla shale bitumen extracts. (B)  $\text{N}_2$ -Ar cross-plot highlighting their origin in the studied gas seeps. The  $\text{N}_2$  and Ar concentrations suggest their atmospheric origin.

Hot meteoric water circulating in the sandstone aquifers beneath the Mut shales likely promotes the catagenetic degradation of the kerogen. This is confirmed by the nitrogen versus argon plot (Fig. 15B), where the nitrogen and argon contents in the gas seeps are comparable to those of air and air-saturated water. Moreover, the  $\delta^{15}\text{N}$  values in the gases in a range close to atmospheric values ( $\delta^{15}\text{N} = 0$ ) confirm the atmospheric origin of  $\text{N}_2$  gases, which were likely mixed with meteoric water in the sandstone aquifers of the Taref, Sabaya and Six Hills Formations. Therefore, we hypothesize that the deep-seated faults act as conduits for hot water and gases circulating in the sandstone aquifers into the overlying Mut shales, resulting in thermal degradation of the sulfur-rich kerogen and generation of the studied gas seeps (Fig. 16). Increasing water content and moisture causes a decrease in the solidity of rocks, which in turn causes variations in temperature through oxidation processes. The water content and inherent moisture content may have an impact on the likelihood of spontaneous combustion<sup>65</sup>.

The research findings demonstrated that a variety of factors work together to generate spontaneous combustion; none of these factors can cause continuous burning, such as that in the study region (Fig. 16). Initially, pyrite is oxidized, which is an exothermic process that creates heat, increasing the reaction rate, and pyrite oxidation results in the precipitation of sulfur and iron. The organic carbon inside the shale then functions as a fuel source for combustion, allowing long-term activity to occur once the requisite ignition temperature is attained. Organic carbon concentrations must be adequate to support combustion, and this research claims that TOC% levels greater than 4% are sufficient to sustain combustion for an extended period of time. When temperatures exceed 100 °C, the moisture content of the oil shale evaporates, causing the shale to expand, become brittle, and crack, increasing the surface area of combustion. A source of oxygen is necessary for combustion to proceed, which may be supplied by air arriving at the shale or by movement of convection water via fissures and cracks.

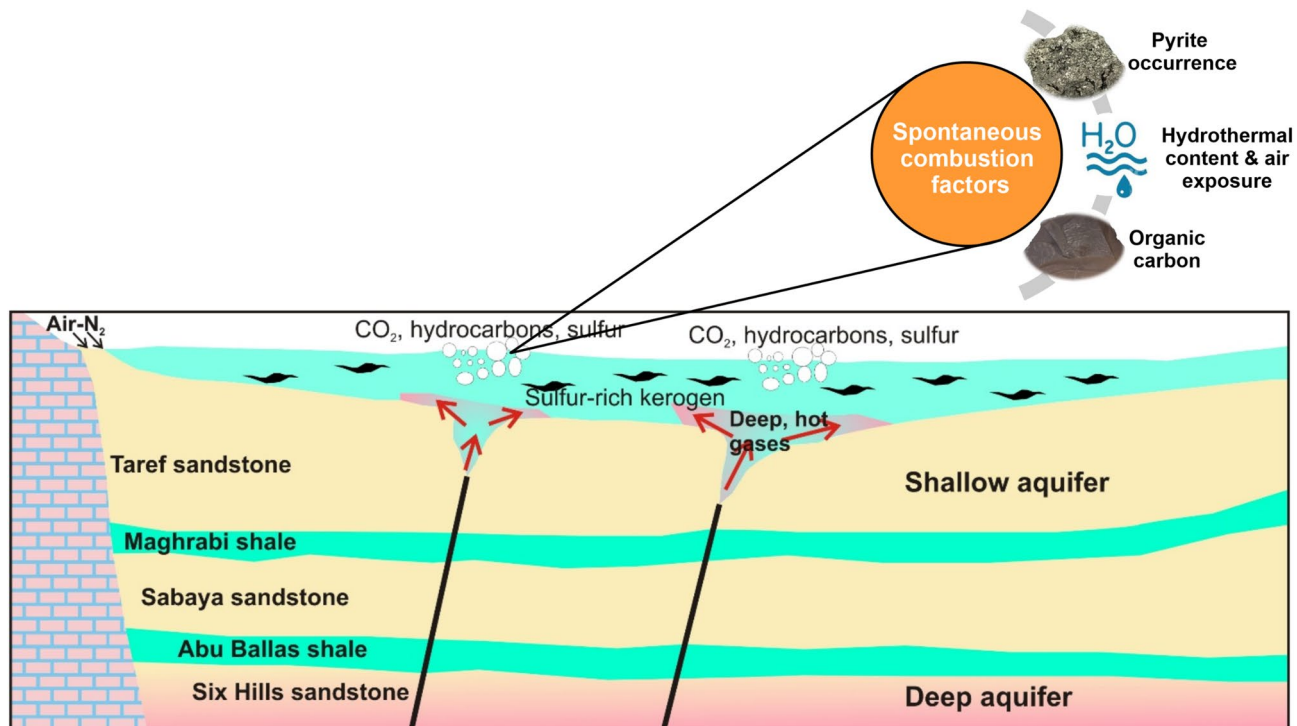


**Figure 16.** Illustrative diagram (not to scale) showing the formation mechanism of the studied gas seeps through a surficial interaction between the organic-rich shales and hot fluids. The interpreted deep-seated faults act as conduits for hot fluids from the deep sandstone aquifers to the surface.

As a result, oxygen flow is a critical aspect in pyrite oxidation and must be well adapted to the initiation and maintenance of combustion.

### Conclusion and recommendation

A strange phenomenon appeared in the village of Al-Hindaw in Dakhla, New Valley Governorate, which was reported by various media. It was the emission of gases and thick smoke rising out of the Earth, which surprised and alarmed everyone in the area. The research region was subjected to field measurements using a variety of geophysical instruments. In addition, geochemical analyses, organic petrography and organic geochemical analysis, as well as gas sampling and analyses, were conducted. Integration of these studies suggested that spontaneous combustion, high temperatures, and gas escape are generated by a combination of factors. Pyrite oxidation by exposure to air or groundwater and organic carbon combustion are two main reasons for continuous spontaneous combustion.

The release of gases and high temperatures in the village of Hindaw is caused by chemical reactions and not by volcanic or seismic activity; thus, there is no reason to be concerned about the stability of the Earth in the research area. The investigation demonstrated the presence of pyrite in the samples taken from the study region in a significant proportion (approximately 20%). Pyrite is an industrial mineral that is used in several industries. To evaluate the economic viability of extracting this mineral, we suggest performing integrated research in the Al-Hindaw region and its vicinity.

Residents of the village of Hindaw and visitors watching this phenomenon must be warned to follow the prohibition and to avoid breathing the produced gases, the majority of which are hydrogen sulfide gas, since inhaling significant quantities of this gas has a detrimental impact on the respiratory and neurological systems. It is advisable to backfill the gas departure area to minimize the escape of gas until optimal use is found (Supplementary information 1, 2 and 3).

### Data availability

The data that support the outcomes of this work are accessible upon reasonable request from the corresponding author.

Received: 12 November 2022; Accepted: 25 September 2023

Published online: 30 September 2023

### References

1. Arnason, B. & Sigurgeirsson, T. Deuterium content of water vapour and hydrogen in volcanic gas at Surtsey, Iceland. *Geochim. Cosmochim. Acta* 32, 807–813. [https://doi.org/10.1016/0016-7037\(68\)90096-3](https://doi.org/10.1016/0016-7037(68)90096-3) (1968).

2. Kiyosu, Y. Hydrogen isotopic compositions of hydrogen and methane from some volcanic areas in north eastern Japan. *Earth Planet. Sci.* **62**, 41–52 (1983).
3. Minissale, A., Evans, W. C., Magro, G. & Vaselli, O. Multiple source components in gas manifestations from north-central Italy. *Chem. Geol.* **142**, 175–192. [https://doi.org/10.1016/s0009-2541\(97\)00081-8](https://doi.org/10.1016/s0009-2541(97)00081-8) (1997).
4. Taran, Y. A., Varley, N. R., Inguaggiato, S. & Cienfuegos, E. Geochemistry of H<sub>2</sub>- and CH<sub>4</sub>-enriched hydrothermal fluids of Socorro Island, Revillagigedo Archipelago, Mexico. Evidence for serpentinization and abiogenic methane. *Geofluids* **10**, 542–555 (2010).
5. Tassi, F., Fiebig, J., Vaselli, O. & Nocentini, M. Origins of methane discharging from volcanic-hydrothermal, geothermal and cold emissions in Italy. *Chem. Geol.* **310–311**, 36–48 (2012).
6. Leila, M. *et al.* Origin of continuous hydrogen flux in gas manifestations at the Larderello geothermal field Central Italy. *Chem. Geol.* **585**, 120564. <https://doi.org/10.1016/j.chemgeo.2021.120564> (2021).
7. E.G.P.C. and CONOCO Coral Company. *Geological Map of Egypt, Scale 1: 500,000* (Cairo, Egypt, 1987).
8. D'Amore, F. & Truesdell, A. Helium in the larderello geothermal fluid. *Geothermics* **13**, 227–239. [https://doi.org/10.1016/0375-6505\(84\)90018-x](https://doi.org/10.1016/0375-6505(84)90018-x) (1984).
9. Chiodini, G. *et al.* Carbon dioxide degassing at Latera caldera (Italy): Evidence of geothermal reservoir and evaluation of its potential energy. *J. Geophys. Res.* **112**, B12204. <https://doi.org/10.1029/2006jb004896> (2007).
10. Etiopie, G. *et al.* Methane and hydrogen in hyperalkaline groundwaters of the serpentinized Dinaride ophiolite belt Bosnia and Herzegovina. *Appl. Geochem.* **84**, 286–296. <https://doi.org/10.1016/j.apgeochem.2017.07.006> (2017).
11. Takaku, J., Tadono, T., Tsutsui, K. & Ichikawa, M. in *IGARSS2018, IEEE*. 1612–1615.
12. El-Kammar, M. M. *Stratigraphical and Mineralogical Studies on the Black Shale at Quseir Area, Red Sea Coast, Egypt* M.Sc thesis, Cairo University (1987).
13. Morgan, P., Boulos, F. K. & Swanberg, C. A. Regional geothermal exploration in Egypt\*. *Geophys. Prospect.* **31**, 361–376. <https://doi.org/10.1111/j.1365-2478.1983.tb01059.x> (1983).
14. Farouk, S., Jain, S., Al-Kahtany, K., Ahmad, F. & Abdeldaim, A. Relationship of maastrichtian-thenetian benthic foraminiferal species diversity, palaeoxygenation, and palaeoproductivity in shallow waters of the Western Desert, Egypt. *Geo Mar. Lett.* **43**, 4 (2023).
15. Brookes, I. A. Geomorphology and quaternary geology of the Dakhla oasis region, Egypt. *Quatern. Sci. Rev.* **13**, 529–552 (1993).
16. Said, R. *The Geology of Egypt* 377 (Elsevier Scientific Publishing Co, 1962).
17. Thorwehe, U. *The Geology of Egypt* 601–614 (The American University in Cairo Press, 1990).
18. Said, R. New light on the origin of the qattara depression. *Bull. Soc. Geograph. Egypt.* **33**, 37–44 (1960).
19. Klitzsch, E., Harms, J. C., Lejal-Nicol, A. & List, F. K. Major subdivisions and depositional environments of Nubia strata south-western Egypt. *AAPG Bull.* **63**, 8. <https://doi.org/10.1306/2f9184aa-16ce-11d7-8645000102c1865d> (1979).
20. Zaher, A. M., Saadi, N. M. & Watanabe, K. Geological applications potential of DEM, ETM+, and gravity data in arid and semi-arid regions with special reference to south Western Desert, Egypt. *Arab. J. Geosci.* **7**, 1705–1716 (2014).
21. Rabeh, T., Bedair, S. & Zaher, A. M. Structural control of hydrogeological aquifers in the Bahariya Oasis Western Desert Egypt. *Geosci. J.* **22**, 145–154 (2018).
22. Zaher, A. M. *et al.* Crustal thermal structure of the Farafra oasis, Egypt, based on airborne potential field data. *Geothermics* **75**, 220–234 (2018).
23. El-Baz, F. *et al.* Journey to the Gilf Kebir and Uweinat Southwest Egypt. *Geograph. J.* **146**, 51–93. <https://doi.org/10.2307/634069> (1978).
24. <https://geovista.co.uk/wp-content/uploads/2015/01/Water-Quality-Probes-Misc.pdf>.
25. Prinz, L. *et al.* Syn- and post-depositional sand bodies in lignite—the role of coal analysis in their recognition a study from the Frimmersdorf Seam, Garzweiler open-cast mine, western Germany. *Int. J. Coal Geol.* **179**, 173–186. <https://doi.org/10.1016/j.coal.2017.05.014> (2017).
26. Makled, W. A., Mostafa, T. F. & Maky, A. B. F. Mechanism of Late Campanian-Early Maastrichtian oil shale deposition and its sequence stratigraphy implications inferred from the palynological and geochemical analysis. *Egypt. J. Petrol.* **23**, 427–444. <https://doi.org/10.1016/j.ejpe.2014.09.011> (2014).
27. Blakely, R. J. *Potential Theory in Gravity & Magnetic Applications* 464 (Cambridge University Press, 1995).
28. Talwani, M. & Heirtzler, J. R. in *Parks, G. A., Ed., Computers in the mineral industries, Part 1* Vol. 9 464–480 (Geological Sciences, 1964).
29. Geosoft 2014. Geosoft Oasis Montaj Extension – GM-SYS 3D Modelling. Feature Sheet, Geosoft Inc, Toronto, Canada (2014).
30. Pickwin v. 4.0.1.5; Plotrefa v. 2.9.1.6 v. 3.3, SeisImager/2DTM Manual: Version 3.3 (2009). [http://epsc.wustl.edu/~epsc454/manuals/SeisImager2D\\_Manual\\_v3.3.pdf](http://epsc.wustl.edu/~epsc454/manuals/SeisImager2D_Manual_v3.3.pdf)
31. Park, C. B., Miller, R. D. & Xia, J. Multichannel analysis of surface waves. *Geophysics* **64**, 800–808 (1999).
32. Park, C. *et al.* in *SEG Int'l Exposition and 74th Annual Meeting*. 1357–1360 (Society of Exploration Geophysicists).
33. Ryden, N. & Park, C. B. Inversion of surface waves using phase velocity spectra. *Geophysics* **71**, 49–58 (2006).
34. Sairam, B., Rastogi, B. K., Aggarwal, S., Chauhan, M. & Bhone, U. Seismic site characterization using Vs30 and site amplification in Gandhinagar region, Gujarat, India. *Curr. Sci.* **100**, 754–761 (2011).
35. Aldahri, M. *et al.* Surface soil assessment in the Ubhur area, north of Jeddah, western Saudi Arabia, using a multichannel analysis of surface waves method. *J. Geol. Soc. India* **89**, 435–443. <https://doi.org/10.1007/s12594-017-0626-7> (2017).
36. Pezeshk, S. & Zarrabi, M. A new inversion procedure for spectral analysis of surface waves using a genetic algorithm. *Bull. Seismol. Soc. Am.* **95**, 1801–1808. <https://doi.org/10.1785/0120040144> (2005).
37. Okada, H. *Geophysical monograph series* (Society of Exploration Geophysicists (SEG), Tulsa, 2003).
38. Suzuki, H. & Hayashi, K. in *SAGEEP 2003. Proceedings on CD ROM (SUR08)*.
39. Park, C. B. & Miller, R. D. Roadside passive multichannel analysis of surface waves (MASW). *J. Environ. Eng. Geophys.* **13**, 1–11 (2008).
40. Nakamura, Y. A method for dynamic characteristics estimation of subsurface using microtremor on the ground surface. 25–33 (Japanese National Railway Technical Research Institute, 1989).
41. Mendecki, M. J., Bieta, B. & Mycka, M. Determination of the resonance frequency–thickness relation based on the ambient seismic noise records from Upper Silesia Coal Basin. *Contemp. Trends Geosci.* **3**, 41–51. <https://doi.org/10.2478/ctg-2014-0021> (2014).
42. Aldahri, M., El-Hadidy, M., Zahran, H. & Abdelrahman, K. Seismic microzonation of Ubhur district, Jeddah, Saudi Arabia, using H/V spectral ratio. *Arab. J. Geosci.* **11**, 113–119. <https://doi.org/10.1007/s12517-018-3415-8> (2018).
43. Alamri, A., Bankher, A., Abdelrahman, K., El-Hadidy, M. & Zahran, H. Soil site characterization of Rabigh city, western Saudi Arabia coastal plain, using HVSR and HVSR inversion techniques. *Arab. J. Geosci.* **13**, 1–6 (2020).
44. SESAME European Research Project WP12. Guidelines for the Implementation of the H/V Spectral Ratio Technique on Ambient Vibrations: Measurements, Processing and Interpretation, 1–62 (2004)
45. ZondTEM1D, Program for one-dimensional data interpretation of transient electromagnetic method using arbitrary source-receiver configuration (loop/line/dipole) v. 5.2 (2016).
46. VLF2DMF, a program for 2-D inversion of multifrequency VLF-EM data v. 1.6 (EMTOMO, 2016). <https://www.geophysik.uni-muenchen.de/~jowa/ManualVLF2D-v106.pdf>
47. Karous, M. & Hjelt, S. E. Linear filtering of Vlf dip-angle measurements\*. *Geophys. Prospect.* **31**, 782–794. <https://doi.org/10.1111/j.1365-2478.1983.tb01085.x> (1983).

48. Bernard, B. B., Brooks, J. M. & Sackett, W. M. Light hydrocarbons in recent Texas continental shelf and slope sediments. *J. Geophys. Res.* **83**, 4053–4061. <https://doi.org/10.1029/JC083iC08p04053> (1978).
49. Schoell, M. The hydrogen and carbon isotopic composition of methane from natural gases of various origins. *Geochim. Cosmochim. Acta* **44**, 649–661. [https://doi.org/10.1016/0016-7037\(80\)90155-6](https://doi.org/10.1016/0016-7037(80)90155-6) (1980).
50. Whiticar, M. J. Carbon and hydrogen isotope systematics of bacterial formation and oxidation of methane. *Chem. Geol.* **161**, 291–314. [https://doi.org/10.1016/S0009-2541\(99\)00092-3](https://doi.org/10.1016/S0009-2541(99)00092-3) (1999).
51. Leila, M. & Moscarillo, A. Organic geochemistry of oil and natural gas in the West Dikrnis and El-Tamad Fields, Onshore Nile Delta, Egypt: Interpretation of potential source rocks. *J. Petrol. Geol.* **40**, 37–58. <https://doi.org/10.1111/jpg.12663> (2017).
52. Radwan, A. A., Nabawy, B. S., Shihata, M. & Leila, M. Seismic interpretation, reservoir characterization, gas origin and entrapment of the Miocene-Pliocene Mangaa C sandstone, Karewa Gas Field, North Taranaki Basin New Zealand. *Marine and Petroleum Geology* **135**, 105420. <https://doi.org/10.1016/j.marpetgeo.2021.105420> (2022).
53. Liu, Q. *et al.* Carbon and hydrogen isotopes of methane, ethane, and propane: A review of genetic identification of natural gas. *Earth Sci. Rev.* **190**, 247–272. <https://doi.org/10.1016/j.earscirev.2018.11.017> (2019).
54. Dakhnov, V. N. Geophysical well logging. *Q. Colorado Sch. Mines* **572**, 445 (1962).
55. Elbarbary, S., Zaher, A. M., Mesbah, H., El-Shahat, H. & Embaby, A. Curie point depth, heat flow and geothermal gradient maps of Egypt deduced from aeromagnetic data. *Renew. Sustain. Energy Rev.* **91**, 620–629 (2018).
56. Mohamed, H. S. *et al.* Correlation of aerogravity and BHT data to develop a geothermal gradient map of the northern western desert of Egypt using an artificial neural network. *Pure Appl. Geophys.* **172**, 1585–1597 (2015).
57. Hunt, J. M. *Petroleum Geochemistry and Geology* (W.H Freeman and Company, 1996).
58. Fang, R. *et al.* Changes of composition and content of tricyclic terpane, hopane, sterane, and aromatic biomarkers throughout the oil window: A detailed study on maturity parameters of lower Toarcian Posidonia shale of the hils syncline NW Germany. *Organ. Geochem.* **138**, 103928. <https://doi.org/10.1016/j.orggeochem.2019.103928> (2019).
59. Zhao, Z., Littke, R., Zieger, L., Hou, D. & Froidl, F. Depositional environment, thermal maturity and shale oil potential of the Cretaceous Qingshankou Formation in the eastern Changling Sag, Songliao Basin, China: An integrated organic and inorganic geochemistry approach. *Int. J. Coal Geol.* **232**, 103621. <https://doi.org/10.1016/j.coal.2020.103621> (2020).
60. Waldo, G. S., Carlson, R. M. K., Moldowan, J. M., Peters, K. E. & Penner-hahn, J. E. Sulfur speciation in heavy petroleum: Information from x-ray absorption near-edge structure. *Geochim. Cosmochim. Acta* **55**, 801–814. [https://doi.org/10.1016/0016-7037\(91\)90343-4](https://doi.org/10.1016/0016-7037(91)90343-4) (1991).
61. Peters, K. E., Walters, C. C. & Moldowan, J. M. *The Biomarker Guide* (Cambridge University Press, 2005).
62. Aizenshtat, Z. & Amrani, A. Significance of  $\delta^{34}\text{S}$  and evaluation of its imprint on sedimentary organic matter: I. The role of reduced sulfur species in the diagenetic stage: A conceptual review. *Geochem. Soc. Special Publ.* **9**, 15–33. [https://doi.org/10.1016/S1873-9881\(04\)80004-X](https://doi.org/10.1016/S1873-9881(04)80004-X) (2004).
63. Kelemen, S. R., Sansone, M., Walters, C. C., Kwiatak, P. J. & Bolin, T. Thermal transformations of organic and inorganic sulfur in type II kerogen quantified by S-XANES. *Geochim. Cosmochim. Acta* **83**, 61–78. <https://doi.org/10.1016/j.gca.2011.12.015> (2012).
64. Shanmugam, G. Significance of coniferous rain forests and related organic matter in generating commercial quantities of oil, Gippsland Basin Australia. *Australia AAPG Bull.* **69**, 1241–1254 (1985).
65. Onifade, M. & Genc, B. Spontaneous combustion liability of coal and coal-shale: A review of prediction methods. *Int. J. Coal Sci. Technol.* **6**, 151–168 (2019).

## Acknowledgements

We would like to express our sincere gratitude and appreciation to Major General Mohammad Al-Zamlout, Governor of the New Valley, and Dr. Nabil Hanafi, Head of the Dakhla Center and city, for their support and facilities throughout the fieldwork. Additionally, we would like to extend our gratitude to Mr. Mahmoud Mahran, a resident of Dakhla city, for the information that he shared with us on the history of this phenomenon.

## Author contributions

M.A.Z.: develop the idea, conduct surveys, processing the data, methodology, visualization, supervision, writing original draft; M.E.: develop the idea, conduct surveys, methodology, writing original draft; G.Q.: develop the idea, resources, supervision, reviewing and editing; T.R.: conduct surveys, supervision, methodology, writing original draft; M.A.: develop the idea, resources, supervision, reviewing and editing; S.E.: supervision, methodology, writing original draft; A.Z.T.: arrange different sections of the manuscript especially the geology and structure parts, writing, reviewing and editing; I.E.: resources, supervision and reviewing; M.A.D.: conduct surveys, methodology, writing original draft; A.A.: conduct surveys, methodology; H.S.: conduct surveys, methodology; M.M.K.: conduct surveys, methodology; M.L.: arrange different sections of the manuscript especially the Geochemical study parts, writing, reviewing and editing.

## Funding

Open access funding provided by The Science, Technology & Innovation Funding Authority (STDF) in cooperation with The Egyptian Knowledge Bank (EKB).

## Competing interests

The authors declare no competing interests.

## Additional information

**Supplementary Information** The online version contains supplementary material available at <https://doi.org/10.1038/s41598-023-43492-1>.

**Correspondence** and requests for materials should be addressed to M.A.Z.

**Reprints and permissions information** is available at [www.nature.com/reprints](http://www.nature.com/reprints).

**Publisher's note** Springer Nature remains neutral with regard to jurisdictional claims in published maps and institutional affiliations.



**Open Access** This article is licensed under a Creative Commons Attribution 4.0 International License, which permits use, sharing, adaptation, distribution and reproduction in any medium or format, as long as you give appropriate credit to the original author(s) and the source, provide a link to the Creative Commons licence, and indicate if changes were made. The images or other third party material in this article are included in the article's Creative Commons licence, unless indicated otherwise in a credit line to the material. If material is not included in the article's Creative Commons licence and your intended use is not permitted by statutory regulation or exceeds the permitted use, you will need to obtain permission directly from the copyright holder. To view a copy of this licence, visit <http://creativecommons.org/licenses/by/4.0/>.

© The Author(s) 2023